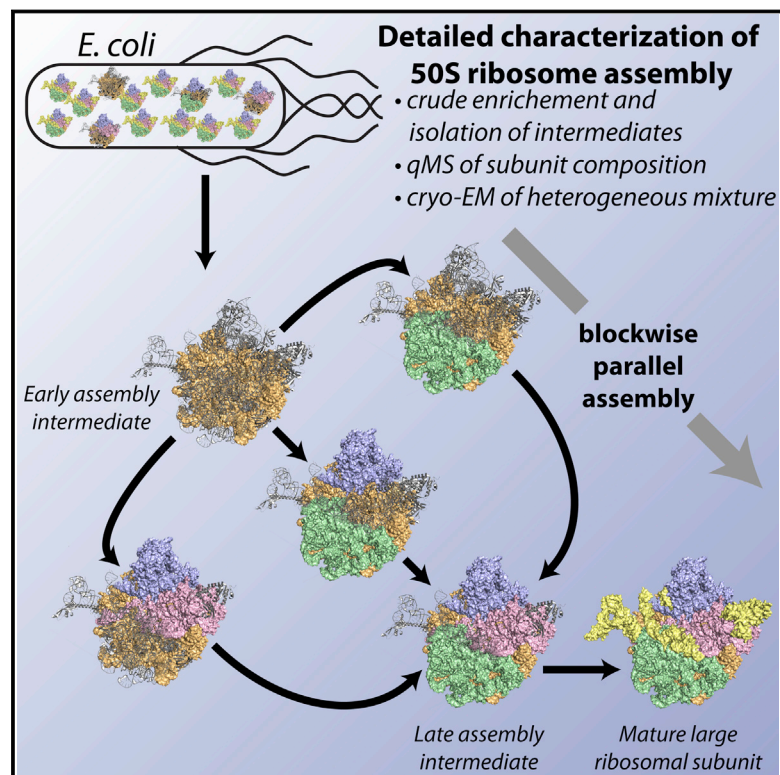# Modular Assembly of the Bacterial Large Ribosomal Subunit

Graphical Abstract

Authors
Joseph H. Davis, Yong Zi Tan,
Bridget Carragher, Clinton S. Potter,
Dmitry Lyumkis, James R. Williamson

Correspondence
dlyumkis@salk.edu (D.L.),
jrwill@scripps.edu (J.R.W.)

In Brief
Assembly pathways for large
macromolecular complexes can be
determined using a combination of
quantitative mass spectrometry and
cryo-EM.

Highlights

- Single-particle cryo-EM and quantitative mass spectrometry of assembling ribosomes

- Ribosome assembly occurs through the coordinated folding of RNA and protein "blocks"

- The order of ribosomal protein association is highly flexible and can be "re-routed"

- Limitation of a single ribosomal protein has long-range structural effects

CellPress

Modular Assembly of the Bacterial Large Ribosomal Subunit

Joseph H. Davis,[1,5] Yong Zi Tan,[2,3,5] Bridget Carragher,[2,3] Clinton S. Potter,[2,3] Dmitry Lyumkis,[4,*] and James R. Williamson[1,6,*]

[1]Department of Integrative Structural and Computational Biology, Department of Chemistry, and The Skaggs Institute for Chemical Biology, The Scripps Research Institute, La Jolla, CA 92037, USA
[2]National Resource for Automated Molecular Microscopy, Simons Electron Microscopy Center, New York Structural Biology Center, New York, NY 10027, USA
[3]Department of Biochemistry and Molecular Biophysics, Columbia University, New York, NY 10032, USA
[4]Laboratory of Genetics and Helmsley Center for Genomic Medicine, The Salk Institute for Biological Studies, La Jolla, CA 92037, USA
[5]Co-first author
[6]Lead Contact
*Correspondence: dlyumkis@salk.edu (D.L.), jrwill@scripps.edu (J.R.W.)
http://dx.doi.org/10.1016/j.cell.2016.11.020

SUMMARY

The ribosome is a complex macromolecular machine and serves as an ideal system for understanding biological macromolecular assembly. Direct observation of ribosome assembly in vivo is difficult, as few intermediates have been isolated and thoroughly characterized. Herein, we deploy a genetic system to starve cells of an essential ribosomal protein, which results in the accumulation of assembly intermediates that are competent for maturation. Quantitative mass spectrometry and single-particle cryo-electron microscopy reveal 13 distinct intermediates, which were each resolved to ~4–5 Å resolution and could be placed in an assembly pathway. We find that ribosome biogenesis is a parallel process, that blocks of structured rRNA and proteins assemble cooperatively, and that the entire process is dynamic and can be "re-routed" through different pathways as needed. This work reveals the complex landscape of ribosome assembly in vivo and provides the requisite tools to characterize additional assembly pathways for ribosomes and other macromolecular machines.

INTRODUCTION

Macromolecular complex assembly involves the synthesis and assembly of defined sets of proteins, RNAs, lipids, and other ligands into a functional superstructure, and understanding the underlying principles of this process remains a significant challenge. Indeed, molecular structures of individual components or complete assemblages are inadequate to infer the preferred in vivo assembly pathway. In addition, it is difficult to determine whether assembly proceeds in an obligate linear fashion or is parallel and flexibly allows for incorporation of elements in an arbitrary order.

The ribosome, which is responsible for protein synthesis in all living organisms, is a complex composite of RNA and protein, and due to the metabolic load associated with ribosome biogenesis, its assembly is under strong selective pressure for efficiency and precision. In bacteria, the primary ~5 kb transcript is cleaved into three component rRNAs, undergoes extensive post-transcriptional modification, and folds into ~150 helices that form ~600 precise tertiary RNA contacts (Petrov et al., 2014). The rRNA processing and folding occurs co-transcriptionally, along with the translation, modification, folding, and binding of ~50 ribosomal proteins, and the entire process is facilitated by the chaperoning activity of ~100 ribosome biogenesis assembly factors and rRNA and r-protein modification enzymes (Shajani et al., 2011). The mature 70S ribosome (Ban et al., 2000) is composed of a small subunit (30S, SSU) and a large subunit (50S, LSU) that essentially assemble independently. Despite this incredible complexity, the bacterial ribosome assembles in ~2 min, with each cell generating ~100,000 ribosomes/hr (Chen et al., 2012). As a result, ribosome assembly intermediates are extremely short-lived and difficult to isolate or characterize directly under rapid growth conditions.

To enrich for intermediates, ribosome assembly can be stalled either genetically (Shajani et al., 2011) or chemically (Stokes et al., 2014), and biochemical and structural characterization of these incomplete particles provides insights into the nature of the putative intermediates in the assembly pathway upstream of the block. As applied to the SSU (Sashital et al., 2014; Sykes and Williamson, 2009), this approach has led to a basic model, where rRNA folding and r-protein binding begin at the 5′ end of the transcript and proceed to the 3′ end.

Compared to the SSU, little is known of LSU assembly in vivo due to the LSU's greater complexity, a greater reliance on assembly factors, and more intricately folded rRNA. Many of the LSU precursor particles isolated to date are largely homogeneous or consist of closely related structures in the final stages of assembly (Jomaa et al., 2013; Li et al., 2013a; Ni et al., 2016). Our understanding of early LSU assembly intermediates is primarily derived from pioneering in vitro reconstitution experiments by the Nierhaus group (Herold and Nierhaus, 1987) that established hierarchical assembly of the 50S subunit, with strong
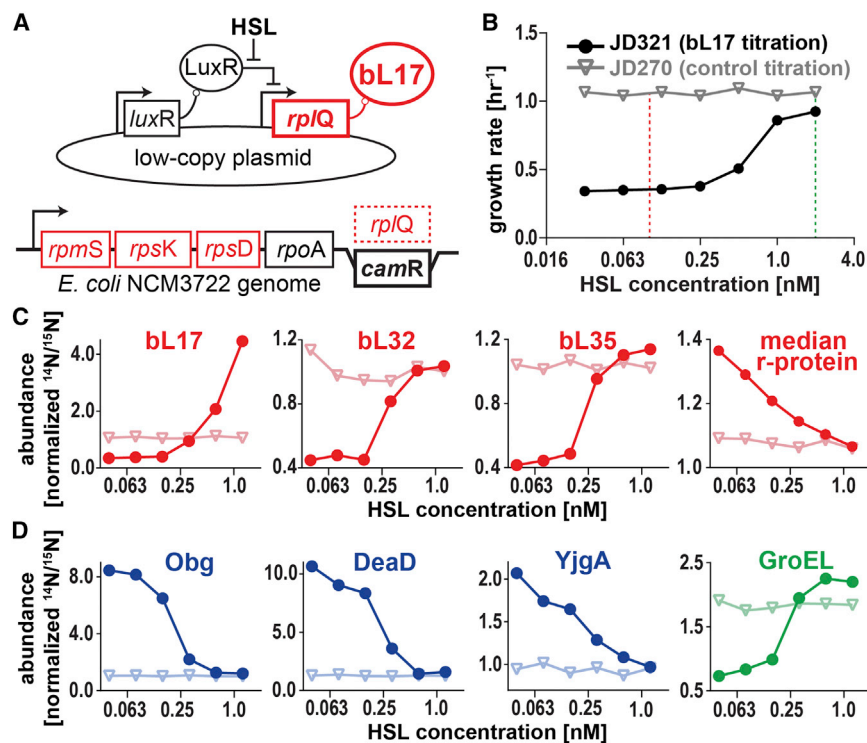
Figure 1. Cellular Response to an R-Protein Limitation

(A) Schematic for the genetic system to regulate the production of bL17. The *rpl*Q gene encoding bL17 (dotted) was replaced with a chloramphenicol resistance gene (*cam*R, bold) using site-specific recombineering. The strain was complemented with a plasmid-borne HSL-inducible copy of *rpl*Q (top). Proteins, coding sequences, and promoters are marked with ovals, rectangles, and arrows, respectively. Ribosomal genes and proteins are colored red.

(B) Growth rate of bL17-titrated (JD321, black circles) and GFP-titrated control (JD270, gray triangles) strains as a function of the HSL inducer concentration. Restrictive (0.1 nM) and permissive (2.0 nM) HSL concentrations used subsequently are noted with vertical red and green dotted lines, respectively.

(C and D) (C) Ribosomal protein and (D) assembly factor or chaperone protein levels as measured by qMS as a function of HSL inducer concentration in bL17-limitation (JD321, dark circles) and control (JD270, light triangles) strains. Traces for ribosomal proteins, assembly factors, and chaperones are colored red, blue, and green, respectively.

thermodynamic cooperativity observed between many of the r-proteins. By withholding sets of r-proteins from the reconstitution reactions, this work revealed the presence of primary proteins, which could bind rRNA independently, and secondary and tertiary proteins, which exhibited improved binding in the presence of primary and secondary proteins, respectively. These distinct classes were consistent with a hierarchical assembly model containing both sequential and parallel pathways, and this model has been critical to our understanding of ribosome biogenesis in vitro.

There are significant differences between ribosome assembly in vivo and in vitro (Shajani et al., 2011), and to better understand the pathways in vivo, we developed a genetic system to deplete a particular ribosomal protein in growing cells, in analogy to omission of an r-protein in the Nierhaus in vitro reconstitution studies. The conserved and essential protein bL17 was chosen for limitation due to its weak primary binding to rRNA and its binding potentiation of a set of other r-proteins in vitro (Herold and Nierhaus, 1987).

Here, we show that limitation of bL17 expression results in the accumulation of a series of incomplete LSU particles, which we establish are competent for maturation using pulse-labeling quantitative mass spectrometry (PL-qMS). We characterize the particles' rRNA conformation using chemical probing, their composition using qMS, and determine the structures of 13 distinct LSU intermediates to ∼4–5 Å resolution using single-particle cryo-electron microscopy (cryo-EM). Unlike prior structural work on the SSU (Mulder et al., 2010; Sashital et al., 2014), the resolution obtained herein allowed for detailed annotation of r-protein and rRNA helix occupancy across the different structures populated in vivo. Using these data, we propose that assembly is highly flexible, taking advantage of multiple accessible pathways to complete assembly when a component is limiting. Notably, progression along these pathways relies on incorporation of cooperative "blocks" of rRNA and bound proteins.

RESULTS

A Genetic System to Perturb Ribosome Biogenesis

The r-protein limitation system was designed to minimally perturb the host chromosome, to provide titratable control of the level of the r-protein of interest, and to ensure a homogeneous response of the entire population of cells to the limitation. Thus, the chromosomal copy of the *rpl*Q gene encoding bL17 was replaced with a cassette (Shoji et al., 2011) intended to minimally disrupt expression of the α-operon, *rps*M-*rps*K-*rps*D-*rpo*A-*rpl*Q, using site-specific recombineering (Datsenko and Wanner, 2000), and this strain was complemented with a plasmid bearing a bL17 expression construct under control of the small molecule N-(β-Ketocaproyl)-L-homoserine lactone (HSL) (Canton et al., 2008) (Figure 1A). The response of a plasmid-borne GFP reporter to the inducer could be accurately titrated without major effects to cellular growth rate (Figure 1B) and, critically, in distinction to *lac*-based (Novick and Weiner, 1957) or *ara*-based (Siegele and Hu, 1997) induction systems, the population of cells responded homogenously (Figure S1A). Titration with HSL induced and eventually saturated GFP expression, with an expression midpoint at 0.3 nM HSL (Figure S1B). Unlike the GFP control strain, the cellular growth rate of the bL17-limitation strain strongly correlated to the level of bL17 produced, consistent
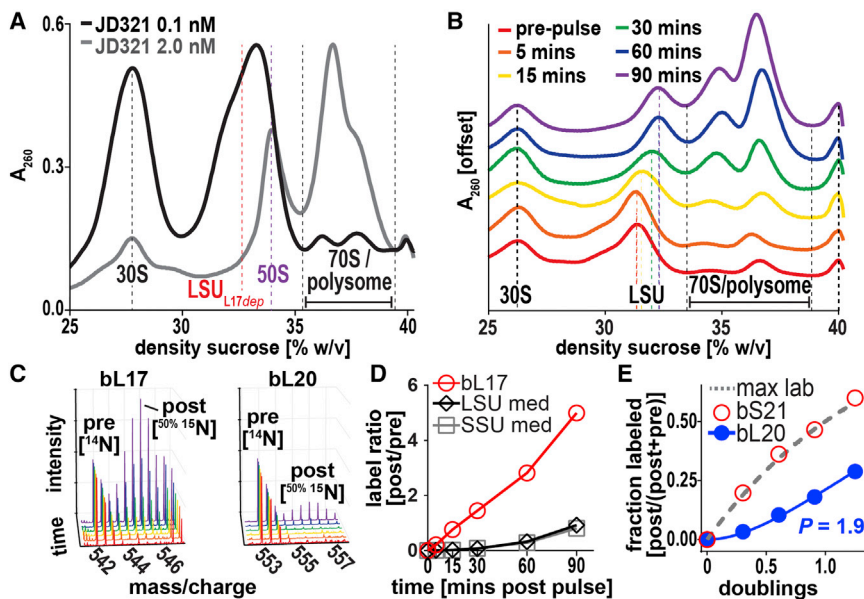
Figure 2. LSU$_{bL17dep}$ Particles Are Maturation-Competent Assembly Intermediates

(A) Sucrose density gradient profiles of JD321 cell lysates grown under restrictive (black) or permissive (gray) conditions. Absorbance at 260 nm, which largely corresponds to rRNA, is plotted, and LSU$_{bL17dep}$ (red), 50S (purple), 30S, and 70S/polysome peaks are marked with vertical dashed lines.

(B) Time course of sucrose density gradient profiles for JD321 cells grown under restrictive conditions after pulsing to permissive conditions. The center of mass for the LSU is noted by the colored dashed lines for each time point harvested pre- and post-pulse. 30S, 70S/polysome, and the bottom of the gradient are marked with black dashed lines.

(C) Representative mass spectra for a bL17 peptide (VVEPLITLAK [47–56]; left) or a bL20 peptide (ILADIAVFDK [94–103]; right) isolated from the 70S fraction post-pulse/bL17-induction as a function of time. Intensities normalized to that of the ^{14}N monoisotopic peak. Colors correspond to time points in (B).

(D) Quantitation of pulsed-isotope label as a function of time post-pulse/bL17 induction. Median peptide value for bL17 (red) and the median LSU (black) or SSU (gray) proteins isolated from 70S particles are plotted at each time point.

(E) Representative 70S particle pulse-labeling kinetics from cells grown under steady-state bL17-limited conditions (0.3 nM HSL). Maximum labeling rate at this cellular growth rate of $\lambda = 0.007$ min^{-1} noted as max lab (dotted gray) and highlighted by bS21 (red), which is known to exchange and will thus label at approximately the growth rate. Kinetic traces were fit as described previously (Chen et al., 2012), resulting in a relative precursor pool size P, which was large for most LSU proteins and consistent with maturation-competent intermediates, as demonstrated by the delayed labeling of representative LSU protein, bL20 (blue).

with its essential function (Figures 1B and 1C) and thereby demonstrating controlled expression of an essential ribosomal protein.

Ribosome Assembly Factors Are Upregulated in Response to Depletion of bL17

To understand the response to an r-protein limitation, the JD321 depletion strain (*E. coli* NCM3722 *rpl*Q::cat, pHSL-*rpl*Q) was grown with differing levels of HSL, and the whole-cell protein composition was determined using qMS. Wild-type (WT) control cells (JD270; *E. coli* NCM3722 pHSL-GFP) in which HSL was used to vary the levels of GFP were also analyzed to identify any proteome changes that were HSL-dependent but bL17-independent. More than 900 proteins (~3,600 peptides) were measured relative to a fixed ^{15}N-labeled reference standard using a SWATH MS^2 quantitation strategy (Gillet et al., 2012). In addition to bL17, the cellular levels of ribosomal proteins bL32 and bL35 were strongly dependent on HSL, consistent with a downregulation of these proteins, as the cells were starved for bL17. Most other ribosomal proteins exhibited small but consistently elevated levels in response to bL17 depletion (Figures 1C and S1D). Inspection of ribosome-associated protein levels revealed upregulation of assembly factors SrmB, DeaD, Obg, RluB, YjgA, and the RNA chaperone CspA, consistent with a cellular response to the induced dysregulation of ribosome biogenesis. Notably, the abundance of multiple protein chaperones, including GroEL, decreased with bL17 depletion (Figures 1D and S1E). Additionally, depletion of bL17 resulted in a dramatic increase in the cellular RNA/protein ratio (Figure S1C), consistent with upregulation of rRNA synthesis in a

similar manner to that observed with ribosome poisons such as chloramphenicol (Scott et al., 2010). Taken together, these data supported a model in which bL17 depletion decreases the cell's translational capacity, resulting in a reduction of the cell's growth rate and need for protein chaperones. In addition, the cell upregulates rRNA synthesis, the expression of ribosomal proteins, and some associated ribosome assembly co-factors.

Depletion of bL17 Perturbs Formation or Maintenance of Mature Ribosomes

Looking more closely at ribosome assembly intermediates, the bL17 depletion strain was grown with either 0.1 or 2.0 nM HSL as restrictive or permissive conditions, respectively. Cells were harvested at mid-log phase, and ribosomal particles were analyzed using sucrose gradient ultracentrifugation (Figure 2A). The restrictive conditions resulted in a clear decrease of 70S particles, with a concomitant increase in 30S particles. A pronounced new peak accumulated in the gradient at ~40S, and, based on the presence of the large subunit (LSU) 23S rRNA, this peak is referred to as LSU$_{bL17dep}$.

The LSU$_{bL17dep}$ Assembly Intermediates Are Competent for Maturation

The LSU$_{bL17dep}$ peak could correspond to degradation products, dead-end assembly products, or intermediates that are competent to mature into 50S subunits. L17-induction-pulse and steady-state pulse-labeling (Chen et al., 2012; Jomaa et al., 2013) experiments were carried out to discriminate among these possibilities.

To chase the LSU$_{bL17dep}$ into 70S ribosomes, an induction-pulse experiment was performed, where bL17-limited cells were simultaneously induced to a level of permissive bL17 expression and pulsed with an isotope label. The growth rate increased from 150 min/doubling pre-pulse to 65 min/doubling post-pulse after a ~15-30 min lag (Figure S2A) accompanied by a gradual disappearance of LSU$_{bL17dep}$ and a concomitant appearance of new 50S and 70S/polysome particles (Figure 2B). These changes outpaced simple dilution from growth, and all of the LSU particles migrated at 50S/70S/polysome within one cell-doubling period. To determine whether the new 70S particles arose from pre-existing LSU$_{bL17dep}$ particles or were synthesized de novo post pulse, label incorporation into the 70S particle was monitored over time on a protein-by-protein basis (Figure 2C). Consistent with the newly formed 70S particles arising from the pre-existing pool of LSU$_{bL17dep}$ particles, significant quantities of pre-pulse isotope-labeled proteins were observed in the 70S peak for the vast majority of both the LSU and SSU proteins (Figure 2C). In contrast, rapid accumulation of post-pulse-labeled bL17 protein was observed within the 70S peak, consistent with the majority of bL17 synthesis taking place after the induction and isotope pulse (Figures 2C and 2D). Pre-existing LSU$_{bL17dep}$ intermediates are thus competent for rapid maturation and join with 30S subunits to form 70S particles and polysomes.

To determine if the LSU$_{bL17dep}$ particle was competent for maturation under steady-state bL17-limiting conditions, cells were grown under bL17-restrictive conditions to mid-log phase and pulsed with isotopically labeled media, and mature 70S particles were isolated and analyzed via mass spectrometry to measure isotope label incorporation as a function of time. For most r-proteins, a clear lag was observed in the kinetics of 70S ribosome labeling relative to the cellular growth rate (Figure 2E), consistent with a model in which the LSU$_{bL17dep}$ particle is part of the 70S precursor pool (Jomaa et al., 2013). As a control, bS21 labeling was monitored because this protein is known to exchange and label at the cellular growth rate irrespective of the precursor pool size (Chen et al., 2012), and the bS21 labeling was clearly distinct from that of other r-proteins (Figure 2E). Fitting the bL20 labeling data to a quantitative model (Chen et al., 2012) revealed a precursor pool size of 1.9 relative to 70S ribosomes, suggesting that the majority of the LSU$_{bL17dep}$ particles were competent for maturation. Taken together, these experiments indicated that the LSU$_{bL17dep}$ particle could rapidly mature upon addition of bL17 and, further, that when limited for bL17, this particle underwent maturation but did so more slowly than under the permissive conditions.

LSU$_{bL17dep}$ Particles Bear Incompletely Processed rRNA

In bacteria, rRNA processing occurs during assembly and has been used as a marker of particle maturity (Stokes et al., 2014; Thurlow et al., 2016). To assess the rRNA processing status in the LSU$_{bL17dep}$ intermediates, next-generation sequencing libraries were generated from LSU intermediates and 70S particles isolated from either bL17-limited or WT cells (see STAR Methods), and the ratio of sequencing reads corresponding to immature versus mature rRNA was calculated for each sample at either the 5′ or 3′ termini. LSU$_{bL17dep}$ particles bore ~4-fold

more incompletely processed 23S rRNA than 70S particles isolated from WT cells (Figures S2B and S2C), consistent with a bL17-depletion-induced processing defect. Additional processing occurred as the LSU$_{bL17dep}$ intermediates matured to 70S particles, as evidenced by the lower levels of unprocessed rRNA. The fact that the LSU$_{bL17dep}$ particles were under-processed relative to their 70S counterparts firmly placed LSU$_{bL17dep}$ upstream of the 70S. Notably, incomplete rRNA processing was observed even in the 70S particles isolated under bL17-limited conditions.

Depletion of bL17 Reorders R-Protein Binding and Particle Assembly

To determine how loss of an essential, early binding r-protein like bL17 impacts ribosome assembly, the protein composition of particles accumulated during bL17 limitation was analyzed. Ribosomal particles from cells grown under either bL17-restrictive or -permissive conditions were fractionated on a sucrose gradient, and the r-protein occupancy relative to a mature 70S particle was determined using qMS. After hierarchical clustering, proteins were assigned to four groups based on their binding profile, with groups I–IV exhibiting progressively delayed binding (Figure 3A). The fact that group IV proteins were completely missing from the LSU$_{bL17dep}$ peak suggested that the binding of these proteins was dependent, directly or indirectly, on bL17, whereas the stoiochiometric binding of group I demonstrated that much of the protein binding in LSU assembly proceeded independently of bL17. Additionally, the partial occupancy observed for group II and III proteins through the 40S region of the gradient indicated that these fractions consisted of a heterogeneous mixture of particles in various stages of assembly. Finally, full occupancy of all r-proteins was observed in the 70S and polysome fractions, indicating that protein bL17 is fully bound in large subunit particles undergoing active translation (Figures 3A and S3B), and these 70S particles were indistinguishable from those assembled under the permissive conditions. The LSU$_{bL17dep}$ occupancy patterns were absent in gradients analyzed from isogenic cells grown under permissive conditions (Figure S3A).

In comparing this dataset to the WT r-protein binding previously determined (Chen and Williamson, 2013), some late-binding proteins were present in the LSU$_{bL17dep}$ particles (e.g., bL12, bL31), while other middle-binding proteins were absent (e.g., bL32). Indeed, coloring the Nierhaus assembly map by these groups (Figure 3B) revealed proteins whose in vivo binding was dependent on bL17 and, furthermore, illustrated a strong reordering of the r-protein binding. This effect was also observed in comparing the r-protein occupancy of a single sucrose gradient fraction isolated either from WT or bL17-restricted cells (Figure S3B). Additionally, the depletion approach allowed for the refinement of the Nierhaus assembly map under in vivo conditions, eliminating some predicted dependencies (blue arrows) and revealing novel direct or indirect binding requirements (red/orange dashed arrows).

The abundance of known ribosome assembly factors was measured through the gradient using qMS, revealing that fractions bearing the LSU$_{bL17dep}$ were strongly enriched for the known assembly co-factors, DeaD, YjgA, RluB, RhlE, and
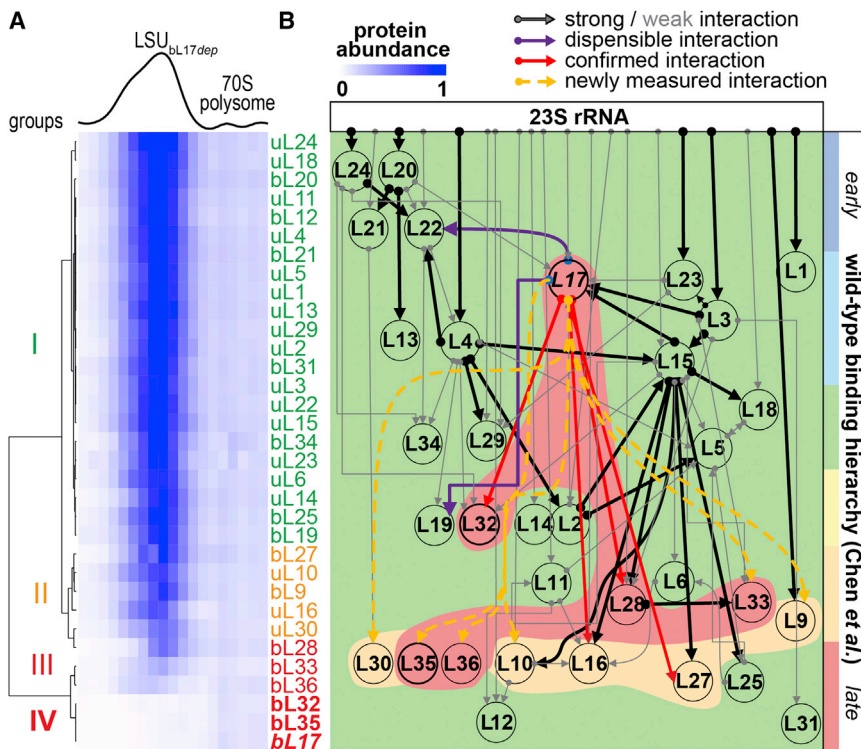
Figure 3. R-Protein Binding Is Re-routed upon bL17 Depletion

(A) Heatmap of LSU protein abundance relative to a purified 70S particle across a sucrose gradient purified from bL17-limited cells (JD321, 0.1 nM HSL). Occupancy patterns were hierarchically clustered to reveal four binding groups, which are marked with proteins labels from earliest (green, I) to latest binding (bold, red, IV). The trace of the sucrose density gradient analyzed is depicted above.

(B) Re-routed Nierhaus assembly map. Proteins are located on the map according to the binding order defined by Chen et al. (2013) from earliest (top) to latest (bottom), and these binding groups are colored at the right side of the map (blue to red). In vitro protein binding cooperativities measured by the Nierhaus group are depicted with thick black (strong cooperativity) or thin gray (weak cooperativity) lines. Interactions that are dispensable for binding in vivo are highlighted purple, whereas those confirmed are colored red. Thick dashed orange lines mark newly measured binding dependencies that are absent from the in vitro map. The assembly map is colored according to the protein binding groups in (A), and bL17 is marked with italics.

YhbY (Figure S3C). We hypothesized that this specific set of factors, which was not enriched in the LSU fractions purified from cells grown under permissive conditions, was likely acting to aid in the assembly of the LSU$_{bL17dep}$ particles and remained associated with the particles due to the bL17-limitation-induced assembly delay.

Native rRNA Secondary Structure Is Present in LSU$_{bL17dep}$ Particles

To assess the status of rRNA folding in the LSU$_{bL17dep}$ particles, sequencing-based RNA chemical probing experiments were performed using the SHAPE-MaP approach (Siegfried et al., 2014). This method was applied to LSU$_{bL17dep}$ particles, 70S particles from WT cells, and protein-free rRNA, and for each particle, a by-residue SHAPE modification value (SR$_{particle}$) was calculated to identify highly reactive residues (see STAR Methods). SHAPE probing of the free 23S rRNA revealed that most residues were unreactive, with highly reactive residues found predominantly in loops and other unpaired structures, similar to that reported previously (Siegfried et al., 2014) (Figure S3D). Calculation of SR$_{bL17}$−SR$_{70SWT}$ revealed that for most residues, the 70S$_{WT}$ and LSU$_{bL17dep}$ reactivity profiles were similar (Figure S3E), suggesting that the vast majority of rRNA secondary structure was formed in the LSU$_{bL17dep}$ particle and is thus formed largely independent of bL17 association. Notably, significant reactivity differences were found near the rRNA termini, likely related to incomplete rRNA processing. More subtle effects were found in portions of the bL17 binding site and the peptidyl transferase center, consistent with altered local structure in these regions.

The LSU$_{bL17dep}$ Peak Is a Heterogeneous Ensemble of Assembly Intermediates

The LSU$_{bL17dep}$ particle bore differing sub-stoichiometric r-protein quantities, suggesting a heterogeneous population of co-purified particles whose average r-protein occupancy was measured by qMS. To determine the structure and composition of the underlying discrete assembly intermediates, we employed single-particle cryo-EM. Briefly, the LSU$_{bL17dep}$ was isolated via sucrose gradient centrifugation, spin-concentrated, and vitrified over holey gold grids, and a cryo-EM dataset of the heterogeneous assembly mixture was collected. Notably, the spin concentration had no effect on the ensemble r-protein occupancy as measured by qMS (Figure S3B).

Individual particles were subjected to an initial round of 3D classification and reconstruction, resulting in 6 different structural super-classes (A–F) ranging in average resolution between 3.7 and 7.9 Å (Table S1 and Figures 4A and S4B). Super-class A resembled a 70S particle missing protein components, and super-class F corresponded to an intact 30S subunit at intermediate resolution. The 30S particle was expected as a tail in the gradient, but the significance of the quasi-70S particle is unclear, and neither super-class A nor F was considered further. A second round of sub-classification and refinement of super-classes C, D, and E resulted in a set of 12 sub-class LSU$_{bL17dep}$ EM density maps at average resolutions of ∼∼4–5 Å. Further classification of these sub-classes or of super-class B did not reveal discernable differences among the resulting maps; however, the presence of residual heterogeneity in these classes could not be excluded.

This 3D classification approach effectively resolved most of the sample heterogeneity, as demonstrated by the 13 disparate
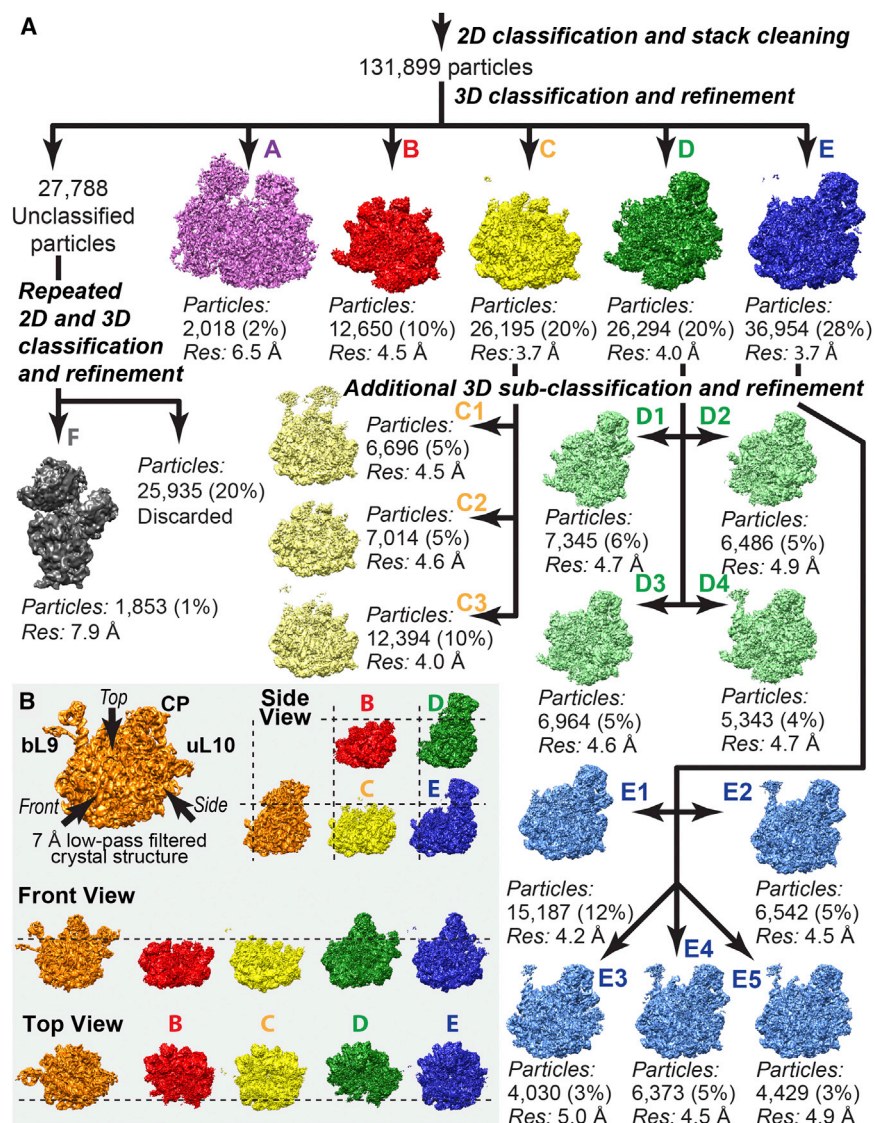
Figure 4. Cryo-EM 3D Classification and Refinement of LSU$_{bL17dep}$ Particles

(A) Particles were classified and refined using a hierarchical scheme (Methods). Annotations indicate number of particles used at each stage of refinement and global map resolution (Res) of the resulting class. Super-classes (A–F), and sub-classes (C1–E5), which resulted from a second round of classification and refinement are depicted.

(B) Side, front, and top views, highlighting EM density missing from each super-class relative to a native 50S subunit. The latter is depicted as EM density using the LSU model from a mature ribosome (PDB: 4YBB). Structures are aligned relative to one another, allowing for direct comparison within each view, as guided by dotted lines.

presence of density for both the CP and the base of the particle and a variable amount of resolved density in the uL1 and uL10/11 stalks as well as the subunit interface.

rRNA and R-Protein Occupancy across the Set of Cryo-EM Maps Reveals Distinct Structures

In each class, most of the observed density could be accounted for using rigid body docking of a mature LSU (PDB: 4YBB). Although the bL17 binding site is apparently formed in all classes (Figure 5A), regions lacking density are distributed over the entire inter-subunit interface, demonstrating wide-ranging effects of bL17 depletion. To facilitate quantitative comparison of the density among the 13 classes, the mature 50S structure was segmented into 109 rRNA helices and 30 r-proteins, and the fractional occupancy of each element was calculated for each class, as described in STAR Methods (Figure S6A). Numerous regions of rRNA structure were missing from the maps of most classes, and given the formation of native secondary structure as measured by SHAPE-MaP, these helices were assumed to be folded but undocked and thus sampling a variety of conformations within a given class. The EM density occupancy values for the ribosomal proteins were largely correlated with aggregate protein abundance levels measured by qMS (Figure S6B), and the strongly uncorrelated proteins (bL9, uL10, and uL11) were localized to the flexible LSU arms (Figure S6C). Overall, the qMS results, which measure the average protein occupancy across all underlying structures irrespective of flexibility or orientation, were consistent with the occupancy results based on individual single-particle cryo-EM reconstructions that allow for a structure-by-structure assessment of proteins bound in their native conformation.

maps. Further, the approach utilized ~80% of identifiable ribosomal particles, indicating that the majority of the underlying structures could be characterized. The maps revealed structures that varied from ~50% of the expected LSU density missing to those that closely resembled fully mature LSUs. Interestingly, density for the solvent side of the LSU was present in all classes, whereas the central protuberance (CP), the inter-subunit interface, and base of the particle were lacking density to varying degrees among the observed classes, and these differences largely distinguished the super-classes B, C, D, and E (Figure 4B). In particular, Class B lacked extensive swaths of density in these regions and represents the least mature LSU intermediate structurally characterized to date. Superclass C bore additional density at the base of the particle, whereas superclass D was defined by the presence of the CP but lacked significant density at the subunit interface along the particle's midline, as well as the base of the particle. Finally, superclass E was notable for the
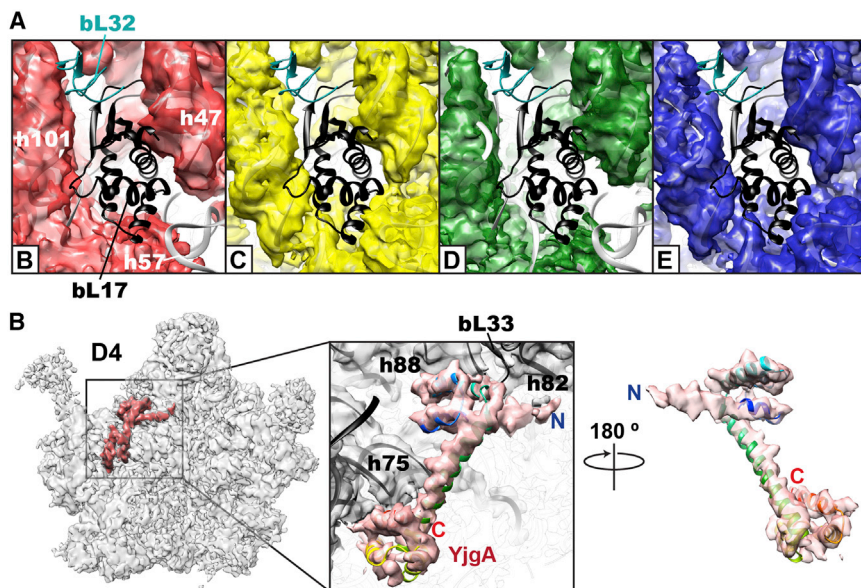
Figure 5. Reconstructed Maps of bL17-Limited Assembly Intermediates

(A) A detailed view of the bL17 binding site. Each superclass (B, C, D, and E) is shown as a colored semi-transparent surface using the color scheme in Figure 4. The docked PDB: 4YBB structure is shown as a gray cartoon model with bL17 and bL32 highlighted in black and cyan, respectively. (B) YjgA bound to the D4 intermediate. Two views of a homology model for the ribosomal cofactor YjgA (rainbow) docked into segmented density (red). Model was calculated using model PDB: 2P0T as the seed on the SWISS-MODEL server. YjgA bears an N-terminal extension relative to the seed model. Proximal LSU elements noted.

Critically, subtle variation within partially resolved regions distinguished the sub-classes (e.g., [D1 versus D2], [E1 versus E2]), supporting their distinct grouping by single-particle classification and leading to the hypothesis that these sub-classes were closely related assembly intermediates representing various stages of assembly progression. Indeed, comparison between classes D1–D4 revealed a monotonic increase in the total volume of the amplitude-scaled maps (Table S1) and a progression toward more native density, which was consistent with related and progressively more mature assembly intermediates.

Given the difference in the apparent maturity of the observed structures, it was logical to attempt to order them into a putative assembly pathway. By both total volume and fraction of native elements resolved, classes B and E5 represent the least and most complete structures, respectively, and they were chosen to represent the earliest and latest intermediates on a putative pathway. Since classes C and D exhibited mutually exclusive association of blocks 2 and 3 (Figure 6A; black box), conversion between any C class and D class would result in loss of native structure. A priori, there is no reason to believe that large amounts of native structure would be formed and lost during assembly, excluding sequential assembly of these classes, which necessarily introduces parallel branches into the general assembly mechanism. Similar mutually exclusive occupancy was found between classes D2–D4 and E1, E2, and E4 (Figure 6A; gray box), introducing an additional branch in the pathway. Finally, occupancy in the C classes was largely a subset of that in the E classes, allowing for conversion of each C class to a cognate E class without the loss of native structure.

Using this information, the classes were assigned an assembly order beginning with the least mature map B and ending in the most mature map E5. For each transition, the number of new structural elements that were formed versus those that were lost was calculated, and the structures were ordered to minimize the number of elements lost during the transitions, the number of required parallel pathways, and the number of classes that could not transition to the terminal E5 class and were ordered to embody a principle of parsimony in the connections depicted (Figures 7 and S7A–S7D). This resulted in three parallel routes

Assembly Factor YjgA Is Bound to a Subset of the bL17-Independent Intermediates

Analyses of whole-cell lysates (Figure S1E) and purified particles (Figure S3C) by qMS suggested that ribosome assembly in bL17-limited cells is, at least in part, reliant on assembly co-factors. Interestingly, a pronounced and well-ordered region of electron density was observed in class D4 that could be assigned as the putative assembly factor YjgA (Figure 5B) (Jiang et al., 2006), which was upregulated upon bL17-limitation and was strongly enriched in the LSU$_{bL17dep}$ particles. Further global classification of each sub-class clearly revealed partial YjgA occupancy in classes D3 and E3 (~30%) and full occupancy in class D4.

Large Subunit Assembly Proceeds through "Limited" Parallel Pathways

Using the occupancy assignments calculated above, the set of structures resulting from EM refinement could be grouped into families of related structures. The quantitative assignment of the fraction of rRNA and proteins in their native conformation for each of the 13 structures allowed for a direct comparison of the "maturity" between each of the classes. As shown in Figure 6A, hierarchical clustering of protein and rRNA helix occupancies identified groups of elements that formed a basis set for the structural differences and grouped the structures according to common elements. The observed EM class groupings were completely consistent with the 3D classification of single-particle images, with each of the C, D, and E sub-classes grouping together. Additionally, the clustering of the rRNA and protein occupancies revealed five major blocks of structural elements (denoted b1–b5) that co-localized on the LSU 3D structure (Figure 6B) and showed differential occupancy between classes. These blocks, which spanned rRNA secondary structure domains, were linked through RNA tertiary contacts (Figure 6C).
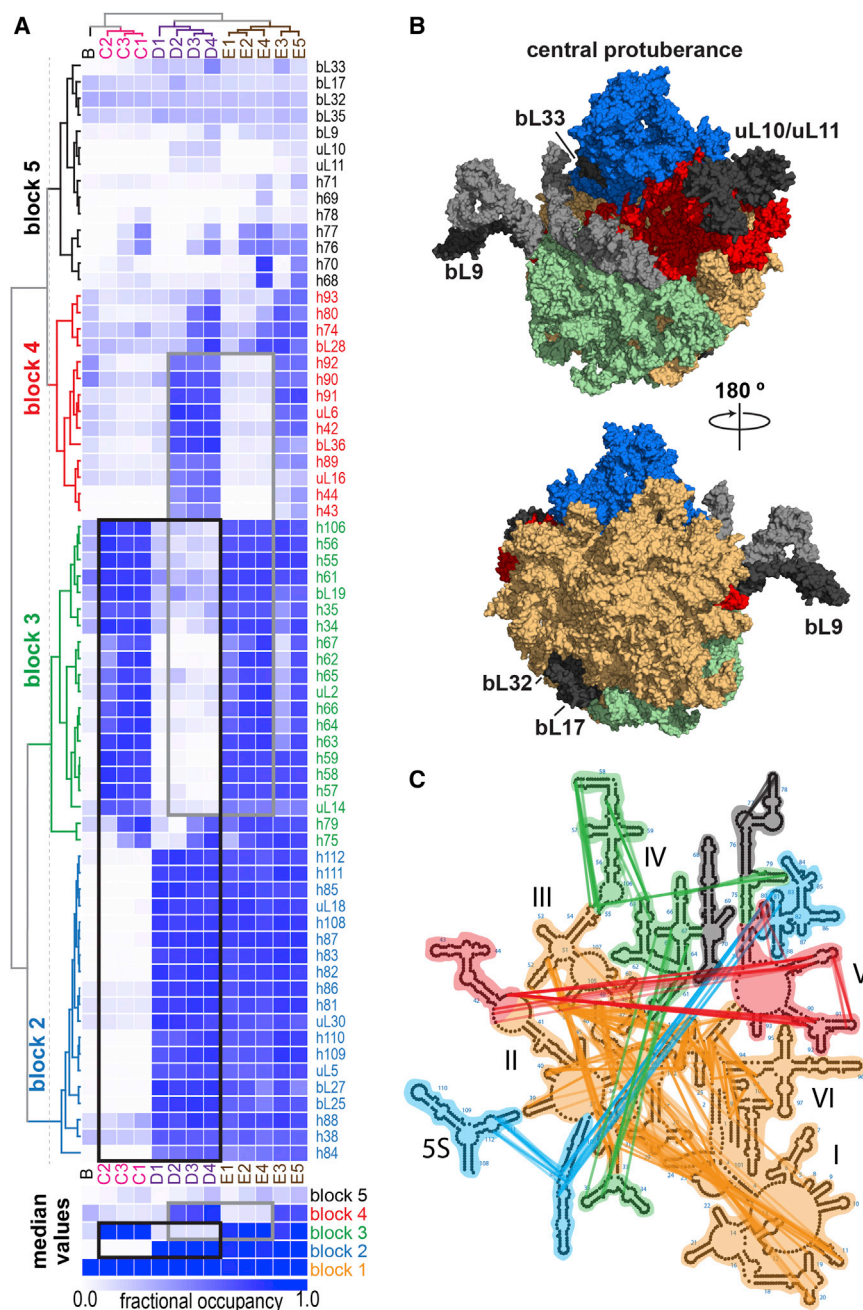
Figure 6. rRNA and R-Protein Cooperative Folding Blocks

(A) Hierarchically clustered heatmap of calculated r-protein and rRNA helix occupancy in different intermediate structures. Values calculated as described in STAR Methods. Blocks 1–5 with coordinated occupancy across different intermediate structures colored orange, blue, green, red, and black, respectively. This color scheme is unrelated to that in Figures 3, 4, or 5. Mutually exclusive blocks highlighted with black and gray rectangles. Occupancy heatmap for block 1 is omitted, as elements are largely present in all structures. For each block, the median occupancy value in each structure is displayed as a heatmap below.

(B) LSU model structure (PDB: 4YBB) with blocks colored according to (A). Block 5 rRNA helices are colored light gray, whereas block 5 proteins missing from all structures are labeled and colored dark gray.

(C) 23S rRNA secondary structure map with rRNA helices colored according to blocks in (A). Colored edges represent tertiary contacts linking helices within blocks.

of assembly that consist of either the C classes, D classes (with E3), or E classes (without E3). This putative assembly pathway represents the first attempt at an assembly map for the 50S subunit with discrete RNA structural transitions.
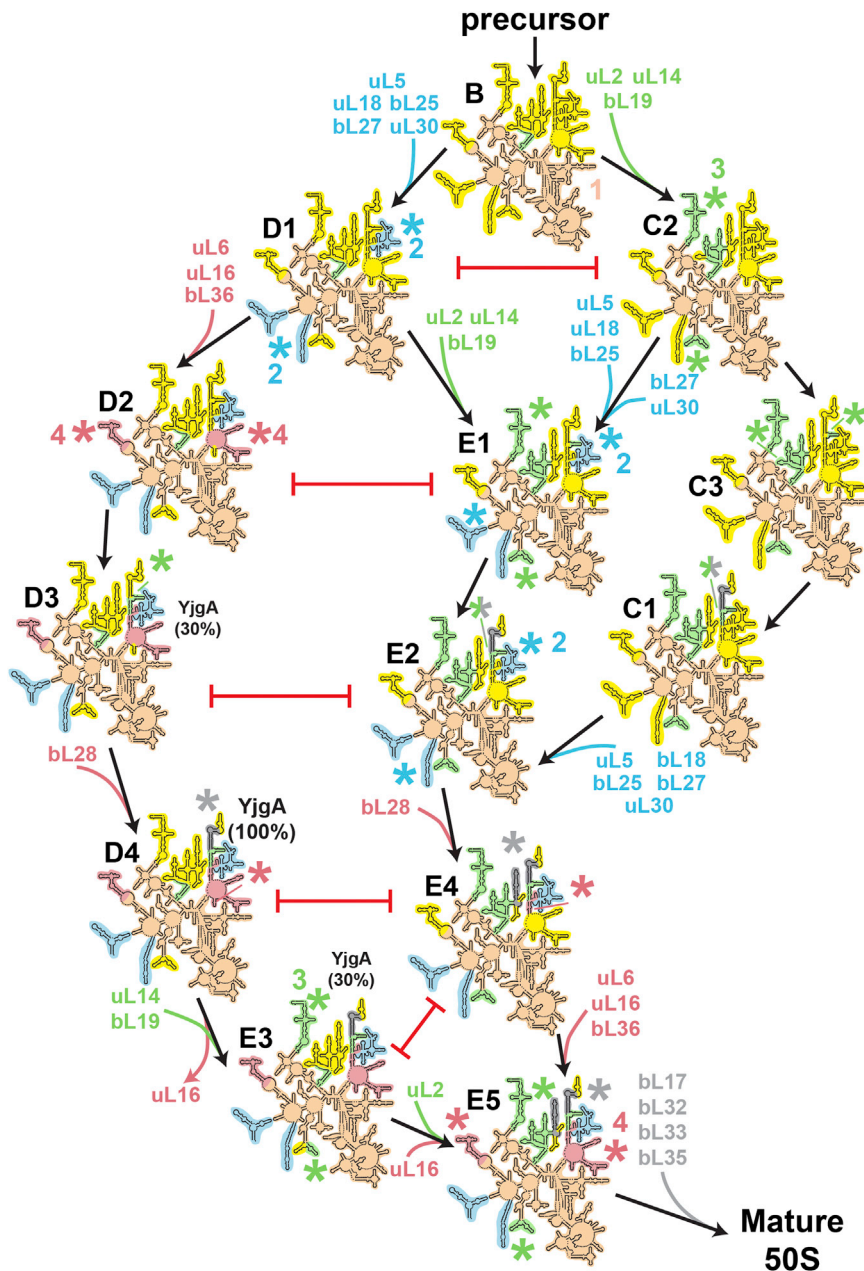
DISCUSSION

Ribosome Biogenesis Utilizes "Limited Parallel Processing" with "Block" Assembly

The hybrid biochemical and structural approach to monitor macromolecular assembly described herein reveals several

notable features of ribosome biogenesis process. First, assembly is highly flexible and can be "re-routed" and allowed to progress even in the absence of the early binding protein, bL17. The existence of such parallel pathways may ensure that blockage of an assembly pathway, for example, due to transient shortages in r-protein availability or rRNA misfolding, results in diversion of ribosome biogenesis flux to alternative pathways until the bottleneck can be relieved. Notably, some components of the 50S subunit are dependent on bL17, including other ribosomal proteins (i.e., bL28, bL32, bL33, bL35) and intersubunit rRNA bridges (e.g., h69, h71). These structures must form downstream of the most mature E5 intermediate class, and their assembly may be rate limiting for overall ribosome biogenesis under the bL17-depletion condition. The fact that proteins "downstream" of bL17 are missing implies that assembly is hierarchical in some regards. However, the presence of very mature rRNA structure and late-binding proteins in the bL17-deficient particles also demonstrates that assembly occurs in parallel and that many portions of the particle can assembly independently. This behavior is denoted as "limited parallel processing," and it has the benefit of affording the maximal flexibility given the thermodynamic constraints of cooperative rRNA folding and r-protein binding.

Second, the hierarchical clustering approach revealed groups of elements with highly correlated behavior across the intermediate

Figure 7. Parallel bL17-Independent Ribosome Assembly Pathways

Putative assembly paths from the least mature B class (top) to the most mature E5 class (bottom). Arrows mark allowed transitions, red lines highlight unfavorable transitions. Unresolved structure is highlighted yellow. Resolved elements are colored by block number as in Figure 6, and element formation is noted with an asterisk (*). Protein binding is shown at each transition. YjgA (black) occupancy percentage is indicated, as calculated by sub-classification in classes D3, D4, and E3.

bly map (Herold and Nierhaus, 1987). These proteins are likely the first bound to 23S rRNA and can each bind independently of bL17. Notably, not all primary binding proteins are in this group, indicating that, in vivo, some proteins require additional components or specific conformations for rapid binding (e.g., uL16, bL28). Finally, specific disruption of the bL17 binding site results in significant long-range structural defects, such as those observed at the peptidyl transferase center (PTC) (Figure S5B), which is located ~90 Å away. This observation provides strong support for the existence of long-range allosteric connections in the ribosome that are important for assembly, just as they are crucial for the process of translation.

Block Assembly Reveals Critical and Dispensable Tertiary rRNA Folding Contacts

Recognition of these independently maturing blocks allowed for identification of tertiary rRNA contacts that span between distinct blocks (Figure S6D) and therefore must be dispensable for folding of at least one of the individual blocks. In some instances, these contacts bridged blocks that exhibit mutually exclusive occupancy between classes, implying that the bridging contact is dispensable for the folding of both blocks (e.g., green/red lines connecting blocks 3 and 4). In other cases, contacts were observed that bridged between one occupied and one unoccupied block (e.g., orange lines emanating from block 1). These contacts must be dispensable for folding of the occupied block but may be important in the folding of the unoccupied block. Identification of which tertiary contacts are within a folding block and which are between folding blocks is impossible from inspection of either the secondary or tertiary structures of the mature 50S subunit and could only be identified by comparison of the set of newly determined assembly intermediate structures.

structures, suggesting that large "blocks" of structure mature in concert as cooperative folding blocks (Figure 6). Notably, these blocks span multiple rRNA secondary structure domains, which are connected through RNA tertiary contacts (Figure 6C) and co-localized on the mature 50S tertiary structure (Figure 6B). For example, block 1, which was present in all structures, consisted exclusively of elements found on the solvent face of the subunit, consistent with this region maturing early during the assembly pathway. The proteins found in block 1 include all of the "early group" primary binding proteins as defined by Chen et al. (2013) (with the exception of bL17), and the majority (9/11) of these proteins are defined as primary binding proteins in the in vitro assem-

The Existence of As-Yet-Unresolved bL17-Dependent Pathways

The bL17-independent assembly pathways describe formation of nearly 50% of the particle, but complete subunit maturation requires the additional incorporation of bL17 and bL17-dependent proteins downstream of class E5. Notably, based on the median r-protein pool size for intermediates, $P = 0.91$, the estimated assembly time through the bL17-independent pathways is ~46 min (Chen et al., 2012), which is ~20-fold slower than under bL17-permissive conditions. This delay could result from slow assembly along the described pathways or from delayed assembly downstream of class E5 as a result of bL17 limitation. This result, and the fact that bL17 is normally an early binding protein, suggests that significant assembly flux progresses through as-yet-unobserved bL17-dependent assembly pathways under optimal growth conditions. Slow but viable assembly pathways, such as those described herein, may exist to allow the cell to cope with ribosome assembly stress brought on by diverse challenges encountered in the wild, such as non-optimal media, temperature, or transient fluctuations in r-proteins and assembly co-factor availability.

Extension of the Nierhaus Large Subunit Assembly Map In Vivo

The structural analysis described here allows an extension of the Nierhaus in vitro assembly map to include the coordinated docking of rRNA helices that accompany binding of r-proteins during assembly in cells. The strong correlation in occupancy between sets of RNA helices and r-proteins in the set of 13 EM maps is consistent with positively cooperative interactions in discrete folding blocks. Using this information, the protein assembly map can be updated to reflect the observed assembly blocks, which include both proteins and rRNA helices (Figures S7E–S7G). Moreover, this information can be used to prune the Nierhaus map of apparent r-protein-binding dependencies that are not strictly necessary in vivo (Figures S7E–S7G, pink arrows). It should be noted that these data simply show that binding of these proteins is possible in the absence of the upstream partner and do not rule out the possibility that binding would be improved were its partner present. Taken together, this work provides a structural basis for the r-protein-binding cooperativity initially observed by the Nierhaus group and provides insight into how folding of blocks of rRNA structure are coupled to r-protein binding.

The Role of Assembly Factors in a Parallel Assembly Pathway

In bacteria, many assembly co-factors are nonessential despite their role in facilitating maturation of the essential ribosome. The parallel pathways revealed herein may help to explain this apparent contradiction, as any given assembly pathway may only require a small subset factors. These parallel pathways provide a level of redundancy such that if a given pathway is blocked by deletion of a factor, greater flux can be shifted to alternative, albeit inherently less efficient pathways. Indeed, nonessential biogenesis co-factors may confer selective advantage by chaperoning a subset of more efficient folding pathways, whereas essential co-factors may facilitate passage through key points of pathway constriction, where inefficiencies in assembly cannot be readily parallelized. Notably, we observe significant occupancy of the putative assembly co-factor YjgA only in a subset of the structures along the D pathway, suggesting that YjgA acts at a late stage of biogenesis and is stably bound exclusively to D-pathway intermediates. Additionally, we find that YjgA occupancy is mutually exclusive with a properly docked helix 68, which is one of the last rRNA elements to mature and forms critical inter-subunit bridges. This finding suggests that YjgA dissociation may act as a signal in the late stages of particle maturation, releasing the mature LSU to bind SSU particles.

Post-translational Regulation of Ribosomal Protein Levels

A subset of proteins (bL32, bL33, and bL35) with low abundance in the LSU$_{bL17dep}$ particles were also depleted in whole-cell lysates (Figures S1D and S3B), implying that free, unincorporated copies of these proteins do not accumulate as would be expected from stoichiometric r-protein expression. Instead, either their synthesis or degradation must be tightly regulated under the restrictive conditions. To distinguish between these possibilities, bL17-limited cells were pulse labeled under steady-state conditions, which revealed significantly slower synthesis of bL32 and bL35 relative to other r-proteins (Figure S2D). In contrast, the synthesis of bL33 was rapid relative to the median LSU r-proteins, and degradation was observed (Figure S2E). Interestingly, both bL32 and bL35 are transcribed using dedicated promoters, whereas bL33 is co-transcribed with bL28, suggesting that the synthesis of bL32 and bL35 is independently downregulated during restrictive conditions whereas the degradation of bL33 is upregulated to produce the appropriate r-protein levels.

The Role of CP Docking in Large Subunit Biogenesis

The observed parallel assembly pathways diverged based in part on the presence or absence of the CP, with the C classes all lacking properly localized CP density. Interestingly, the relatively mature C1 class bore significant density resembling the CP; however, it was rotated and docked adjacent to the uL1 stalk, resulting in a lack of native density for the CP rRNA (5S, helices 82–87) and helices 38 and 68 (Figure S5C). This apparent rotation was not an artifact of errant rigid body docking, as the peptide exit tunnel was observed in the expected location (Figure S5A), and 2D class averages exhibited pronounced CP density in this rotated conformation (Figure S5D). Interestingly, this orientation was reminiscent of that observed previously (Leidig et al., 2014) in eukaryotic pre-60S particles and may represent a common rRNA misfolding trap that spans the prokaryotic and eukaryotic kingdoms. According to our proposed assembly pathway, this kinetic trap is overcome as the C1 class matures to the E2 class, resulting in a properly docked CP relatively late in assembly. In contrast, a properly docked CP is observed in the very immature D1 class, which is significantly less mature than class C1. This result argues that the CP can properly dock even in relatively immature intermediates, such as D1, and suggests that this nonnative conformation is either nonobligatory or is populated very transiently in the B-to-D1 transition. While

class D1 was generally less mature than C1, it did bear properly docked helices 38 and 81–88 whereas class C1 did not. This result is consistent with previous data reviewed in Dontsova and Dinman (2005), implicating these helices in cooperative docking of the 5S rRNA into the CP.

An Evolving Assembly Pathway

A principle tenet of the RNA-world hypothesis is the existence of a primordial RNA-only ribosome bearing a functional peptidyl transferase center (PTC). Indeed, an elegant analysis of structural motifs found in modern ribosomes suggested that the PTC was the first ribosome element to evolve and that additional elements of the 23S were added to this PTC throughout evolution (Bokov and Steinberg, 2009). As PTC is one of the last elements to mature during assembly of a modern ribosome (Figure S5B), the entire order of ribosome assembly must have undergone a drastic rearrangement during evolution and suggests that our understanding of ribosome evolution may be incomplete. Interestingly, the late maturation of the PTC has been observed in the distantly related *B. subtilis* previously (Jomaa et al., 2013), suggesting that this late timing is a conserved feature of the modern ribosome, potentially protecting the cell from peptidyl-transferase-active yet incompletely matured ribosomes.

Hybrid Approaches to Understanding Macromolecular Complex Assembly

The putative assembly pathways enumerated herein highlight how the relative order of ribosomal structure formation can differ depending on the particular kinetic traps encountered by each particle (Figure S7). Identification of these parallel assembly pathways was not possible using bulk measurements, such as qMS or SHAPE-MaP, and required the detailed 3D classification of single-particle EM datasets. The depletion strategy outlined herein can be readily extended to target other ribosomal proteins and should help to elucidate the bL17-dependent pathways. Furthermore, analysis of the relationships of the intermediates that accumulate and the blocks of structure that form under different limitations will allow a more complete understanding of the overall pathway of biogenesis. Additionally, the experimental framework and tools described here should be readily applicable to the study of the biogenesis of other critical macromolecular complexes. Indeed, putative assembly intermediates have been identified by perturbing assembly of various macromolecular complexes including the proteasome (Tomko and Hochstrasser, 2013) and the spliceosome (Matera and Wang, 2014). The described pulse-labeling and qMS techniques should be useful in determining whether the accumulating particles are competent for maturation and in assessing the average composition of the underlying intermediates. When atomic-scale models are available for the complex of interest, our approach to determine the course-grained structure and precise protein-by-protein composition of the vast majority of the particles present in a heterogeneous sample should be of great utility in assessing the degree to which assembly is parallelized and in determining the constituents of various cooperatively folded domains and the relative abundance of assembly intermediates.

STAR★METHODS

Detailed methods are provided in the online version of this paper and include the following:

- KEY RESOURCES TABLE
- CONTACT FOR REAGENT AND RESOURCE SHARING
- METHOD DETAILS
  - Strain construction
  - Purification of ribosome biogenesis related proteins from the ASKA collection
  - Quantitation of growth rates, protein and RNA abundance as a function of HSL
  - Cell growth and isolation of ribosomal particles
  - Preparation of sample for quantitative mass spectrometry
  - Quantitative mass spectrometry of ribosomal proteins and assembly factors
  - Whole cell proteomics
  - Pulse-labeling proteomics
  - SHAPE-MaP based quantitation of rRNA secondary structure
  - Next-generation sequencing based quantitation of rRNA processing
  - Electron microscopy data collection
  - Electron microscopy micrograph pre-processing and particle stack cleaning
  - Electron microscopy density reconstruction, 3D classification, and refinement
  - Quantitation of rRNA and protein occupancy in EM density maps
- QUANTIFICATION AND STATISTICAL ANALYSIS
- DATA AND SOFTWARE AVAILABILITY
- EXPERIMENTAL MODEL AND SUBJECT DETAILS

SUPPLEMENTAL INFORMATION

Supplemental Information includes seven figures and one table and can be found with this article online at http://dx.doi.org/10.1016/j.cell.2016.11.020.

REFERENCES

Ban, N., Nissen, P., Hansen, J., Moore, P.B., and Steitz, T.A. (2000). The complete atomic structure of the large ribosomal subunit at 2.4 A resolution. Science *289*, 905–920.

Bokov, K., and Steinberg, S.V. (2009). A hierarchical model for evolution of 23S ribosomal RNA. Nature *457*, 977–980.

Canton, B., Labno, A., and Endy, D. (2008). Refinement and standardization of synthetic biological parts and devices. Nat. Biotechnol. *26*, 787–793.

Chen, S.S., and Williamson, J.R. (2013). Characterization of the ribosome biogenesis landscape in E. coli using quantitative mass spectrometry. J. Mol. Biol. *425*, 767–779.

Chen, S.S., Sperling, E., Silverman, J.M., Davis, J.H., and Williamson, J.R. (2012). Measuring the dynamics of E. coli ribosome biogenesis using pulse-labeling and quantitative mass spectrometry. Mol. Biosyst. *8*, 3325–3334.

Datsenko, K.A., and Wanner, B.L. (2000). One-step inactivation of chromosomal genes in Escherichia coli K-12 using PCR products. Proc. Natl. Acad. Sci. USA *97*, 6640–6645.

Dontsova, O.A., and Dinman, J.D. (2005). 5S rRNA: Structure and Function from Head to Toe. Int. J. Biomed. Sci. *1*, 1–7.

Eng, J.K., Jahan, T.A., and Hoopmann, M.R. (2013). Comet: an open-source MS/MS sequence database search tool. Proteomics *13*, 22–24.

Gillet, L.C., Navarro, P., Tate, S., Rost, H., Selevsek, N., Reiter, L., Bonner, R., and Aebersold, R. (2012). Targeted data extraction of the MS/MS spectra generated by data-independent acquisition: a new concept for consistent and accurate proteome analysis. MCP *11*, O111 016717.

Grant, T., and Grigorieff, N. (2015). Measuring the optimal exposure for single particle cryo-EM using a 2.6 Å reconstruction of rotavirus VP6. eLife *4*, e06980.

Grigorieff, N. (2016). Frealign: An Exploratory Tool for Single-Particle Cryo-EM. Methods Enzymol. *579*, 191–226.

Gulati, M., Jain, N., Davis, J.H., Williamson, J.R., and Britton, R.A. (2014). Functional interaction between ribosomal protein L6 and RbgA during ribosome assembly. PLoS Genet. *10*, e1004694.

Herold, M., and Nierhaus, K.H. (1987). Incorporation of six additional proteins to complete the assembly map of the 50 S subunit from Escherichia coli ribosomes. J. Biol. Chem. *262*, 8826–8833.

Jiang, M., Datta, K., Walker, A., Strahler, J., Bagamasbad, P., Andrews, P.C., and Maddock, J.R. (2006). The Escherichia coli GTPase CgtAE is involved in late steps of large ribosome assembly. J. Bacteriol. *188*, 6757–6770.

Jomaa, A., Jain, N., Davis, J.H., Williamson, J.R., Britton, R.A., and Ortega, J. (2013). Functional domains of the 50S subunit mature late in the assembly process. Nucleic Acids Res. *42*, 3419–3435.

Keller, A., Nesvizhskii, A.I., Kolker, E., and Aebersold, R. (2002). Empirical statistical model to estimate the accuracy of peptide identifications made by MS/MS and database search. Anal. Chem. *74*, 5383–5392.

Kitagawa, M., Ara, T., Arifuzzaman, M., Ioka-Nakamichi, T., Inamoto, E., Toyonaga, H., and Mori, H. (2005). Complete set of ORF clones of Escherichia coli ASKA library (a complete set of E. coli K-12 ORF archive): unique resources for biological research. DNA Res. *12*, 291–299.

Kucukelbir, A., Sigworth, F.J., and Tagare, H.D. (2014). Quantifying the local resolution of cryo-EM density maps. Nat. Methods *11*, 63–65.

Lam, H., Deutsch, E.W., Eddes, J.S., Eng, J.K., King, N., Stein, S.E., and Aebersold, R. (2007). Development and validation of a spectral library searching method for peptide identification from MS/MS. Proteomics *7*, 655–667.

Leidig, C., Thoms, M., Holdermann, I., Bradatsch, B., Berninghausen, O., Bange, G., Sinning, I., Hurt, E., and Beckmann, R. (2014). 60S ribosome biogenesis requires rotation of the 5S ribonucleoprotein particle. Nat. Commun. *5*, 3491.

Li, N., Chen, Y., Guo, Q., Zhang, Y., Yuan, Y., Ma, C., Deng, H., Lei, J., and Gao, N. (2013a). Cryo-EM structures of the late-stage assembly intermediates of the bacterial 50S ribosomal subunit. Nucleic Acids Res. *41*, 7073–7083.

Li, X., Mooney, P., Zheng, S., Booth, C.R., Braunfeld, M.B., Gubbens, S., Agard, D.A., and Cheng, Y. (2013b). Electron counting and beam-induced motion correction enable near-atomic-resolution single-particle cryo-EM. Nat. Methods *10*, 584–590.

Ludtke, S.J., Baldwin, P.R., and Chiu, W. (1999). EMAN: semiautomated software for high-resolution single-particle reconstructions. J. Struct. Biol. *128*, 82–97.

Lyumkis, D., Brilot, A.F., Theobald, D.L., and Grigorieff, N. (2013a). Likelihood-based classification of cryo-EM images using FREALIGN. J. Struct. Biol. *183*, 377–388.

Lyumkis, D., Vinterbo, S., Potter, C.S., and Carragher, B. (2013b). Optimod–an automated approach for constructing and optimizing initial models for single-particle electron microscopy. J. Struct. Biol. *184*, 417–426.

MacLean, B., Eng, J.K., Beavis, R.C., and McIntosh, M. (2006). General framework for developing and evaluating database scoring algorithms using the TANDEM search engine. Bioinformatics *22*, 2830–2832.

MacLean, B., Tomazela, D.M., Shulman, N., Chambers, M., Finney, G.L., Frewen, B., Kern, R., Tabb, D.L., Liebler, D.C., and MacCoss, M.J. (2010). Skyline: an open source document editor for creating and analyzing targeted proteomics experiments. Bioinformatics *26*, 966–968.

Matera, A.G., and Wang, Z. (2014). A day in the life of the spliceosome. Nat. Rev. Mol. Cell Biol. *15*, 108–121.

Mindell, J.A., and Grigorieff, N. (2003). Accurate determination of local defocus and specimen tilt in electron microscopy. J. Struct. Biol. *142*, 334–347.

Mulder, A.M., Yoshioka, C., Beck, A.H., Bunner, A.E., Milligan, R.A., Potter, C.S., Carragher, B., and Williamson, J.R. (2010). Visualizing ribosome biogenesis: parallel assembly pathways for the 30S subunit. Science *330*, 673–677.

Nesvizhskii, A.I., Keller, A., Kolker, E., and Aebersold, R. (2003). A statistical model for identifying proteins by tandem mass spectrometry. Anal. Chem. *75*, 4646–4658.

Ni, X., Davis, J.H., Jain, N., Razi, A., Benlekbir, S., McArthur, A.G., Rubinstein, J.L., Britton, R.A., Williamson, J.R., and Ortega, J. (2016). YphC and YsxC GTPases assist the maturation of the central protuberance, GTPase associated region and functional core of the 50S ribosomal subunit. Nucleic Acids Res. *44*, 8442–8455.

Novick, A., and Weiner, M. (1957). Enzyme Induction as an All-or-None Phenomenon. Proc. Natl. Acad. Sci. USA *43*, 553–566.

Petrov, A.S., Bernier, C.R., Gulen, B., Waterbury, C.C., Hershkovits, E., Hsiao, C., Harvey, S.C., Hud, N.V., Fox, G.E., Wartell, R.M., and Williams, L.D. (2014). Secondary structures of rRNAs from all three domains of life. PLoS ONE *9*, e88222.

Pintilie, G.D., Zhang, J., Goddard, T.D., Chiu, W., and Gossard, D.C. (2010). Quantitative analysis of cryo-EM density map segmentation by watershed and scale-space filtering, and fitting of structures by alignment to regions. J. Struct. Biol. *170*, 427–438.

Reiter, L., Claassen, M., Schrimpf, S.P., Jovanovic, M., Schmidt, A., Buhmann, J.M., Hengartner, M.O., and Aebersold, R. (2009). Protein identification false discovery rates for very large proteomics data sets generated by tandem mass spectrometry. Mol. Cell. Proteomics *8*, 2405–2417.

Roseman, A.M. (2004). FindEM–a fast, efficient program for automatic selection of particles from electron micrographs. J. Struct. Biol. *145*, 91–99.

Rubinstein, J.L., and Brubaker, M.A. (2015). Alignment of cryo-EM movies of individual particles by optimization of image translations. J. Struct. Biol. *192*, 188–195.

Russo, C.J., and Passmore, L.A. (2014). Electron microscopy: Ultrastable gold substrates for electron cryomicroscopy. Science *346*, 1377–1380.

Sashital, D.G., Greeman, C.A., Lyumkis, D., Potter, C.S., Carragher, B., and Williamson, J.R. (2014). A combined quantitative mass spectrometry and electron microscopy analysis of ribosomal 30S subunit assembly in E. coli. eLife *3*, e04491.

Scheres, S.H. (2012). RELION: implementation of a Bayesian approach to cryo-EM structure determination. J. Struct. Biol. *180*, 519–530.

Scott, M., Gunderson, C.W., Mateescu, E.M., Zhang, Z., and Hwa, T. (2010). Interdependence of cell growth and gene expression: origins and consequences. Science *330*, 1099–1102.

Shajani, Z., Sykes, M.T., and Williamson, J.R. (2011). Assembly of bacterial ribosomes. Annu. Rev. Biochem. *80*, 501–526.

Shoji, S., Dambacher, C.M., Shajani, Z., Williamson, J.R., and Schultz, P.G. (2011). Systematic chromosomal deletion of bacterial ribosomal protein genes. J. Mol. Biol. *413*, 751–761.

Shteynberg, D., Deutsch, E.W., Lam, H., Eng, J.K., Sun, Z., Tasman, N., Mendoza, L., Moritz, R.L., Aebersold, R., and Nesvizhskii, A.I. (2011). iProphet: multi-level integrative analysis of shotgun proteomic data improves peptide and protein identification rates and error estimates. MCP *10*, M111 007690.

Siegele, D.A., and Hu, J.C. (1997). Gene expression from plasmids containing the araBAD promoter at subsaturating inducer concentrations represents mixed populations. Proc. Natl. Acad. Sci. USA *94*, 8168–8172.

Siegfried, N.A., Busan, S., Rice, G.M., Nelson, J.A., and Weeks, K.M. (2014). RNA motif discovery by SHAPE and mutational profiling (SHAPE-MaP). Nat. Methods *11*, 959–965.

Sorzano, C.O., Marabini, R., Velázquez-Muriel, J., Bilbao-Castro, J.R., Scheres, S.H., Carazo, J.M., and Pascual-Montano, A. (2004). XMIPP: a new generation of an open-source image processing package for electron microscopy. J. Struct. Biol. *148*, 194–204.

Sorzano, C.O., Bilbao-Castro, J.R., Shkolnisky, Y., Alcorlo, M., Melero, R., Caffarena-Fernández, G., Li, M., Xu, G., Marabini, R., and Carazo, J.M. (2010). A clustering approach to multireference alignment of single-particle projections in electron microscopy. J. Struct. Biol. *171*, 197–206.

Sperling, E., Bunner, A.E., Sykes, M.T., and Williamson, J.R. (2008). Quantitative analysis of isotope distributions in proteomic mass spectrometry using least-squares Fourier transform convolution. Anal. Chem. *80*, 4906–4917.

Stokes, J.M., Davis, J.H., Mangat, C.S., Williamson, J.R., and Brown, E.D. (2014). Discovery of a small molecule that inhibits bacterial ribosome biogenesis. eLife *3*, e03574.

Sykes, M.T., and Williamson, J.R. (2009). A complex assembly landscape for the 30S ribosomal subunit. Annu. Rev. Biophys. *38*, 197–215.

Thurlow, B., Davis, J.H., Leong, V., F Moraes, T., Williamson, J.R., and Ortega, J. (2016). Binding properties of YjeQ (RsgA), RbfA, RimM and Era to assembly intermediates of the 30S subunit. Nucleic Acids Res. Published online July 5, 2016. http://dx.doi.org/10.1093/nar/gkw613.

Tomko, R.J., Jr., and Hochstrasser, M. (2013). Molecular architecture and assembly of the eukaryotic proteasome. Annu. Rev. Biochem. *82*, 415–445.

Voss, N.R., Yoshioka, C.K., Radermacher, M., Potter, C.S., and Carragher, B. (2009). DoG Picker and TiltPicker: software tools to facilitate particle selection in single particle electron microscopy. J. Struct. Biol. *166*, 205–213.

Zhang, K. (2016). Gctf: Real-time CTF determination and correction. J. Struct. Biol. *193*, 1–12.

STAR★METHODS

KEY RESOURCES TABLE

REAGENT or RESOURCE	SOURCE	IDENTIFIER
Chemicals, Peptides, and Recombinant Proteins		
Purified Aska proteins	This paper	N/A
N-(β-Ketocaproyl)-L-homoserine lactone	Santa Cruz Biotech.	Cat#: sc-205396
G-50 microspin columns	GE Healthcare	Cat#: 27533001
Random Primer 9	New England BioLabs	Cat#: S1254S
1-methyl-7-nitroisatoic anhydride	This paper	N/A
Deposited Data		
Quantitative mass spectrometry data tables	This paper	https://github.com/williamsonlab/Davis_Tan_2016/tree/master/qMS_data_sets
Table of ASKA purified proteins	This paper	https://github.com/williamsonlab/Davis_Tan_2016/tree/master/aska
Cryo-EM density map: Class A	This paper	EMD: 8434
Cryo-EM density map: Class B	This paper	EMD: 8440
Cryo-EM density map: Class C	This paper	EMD: 8441
Cryo-EM density map: Class C1	This paper	EMD: 8442
Cryo-EM density map: Class C2	This paper	EMD: 8443
Cryo-EM density map: Class C3	This paper	EMD: 8444
Cryo-EM density map: Class D	This paper	EMD: 8445
Cryo-EM density map: Class D1	This paper	EMD: 8446
Cryo-EM density map: Class D2	This paper	EMD: 8447
Cryo-EM density map: Class D3	This paper	EMD: 8448
Cryo-EM density map: Class D4	This paper	EMD: 8449
Cryo-EM density map: Class E	This paper	EMD: 8450
Cryo-EM density map: Class E1	This paper	EMD: 8451
Cryo-EM density map: Class E2	This paper	EMD: 8452
Cryo-EM density map: Class E3	This paper	EMD: 8453
Cryo-EM density map: Class E4	This paper	EMD: 8455
Cryo-EM density map: Class E5	This paper	EMD: 8456
Cryo-EM density map: Class F	This paper	EMD: 8457
Cryo-EM raw particle stack	This paper	EMPIAR: 10076
Experimental Models: Organisms/Strains		
JD321: *E. coli* NCM3722 [rplQ::cat, pJD075]	This paper	N/A
JD270: *E. coli* NCM3722 [pJD036]	This paper	N/A
JD189: *E. coli* NCM3722	Terry Hwa Lab	N/A
Recombinant DNA		
pJD036 [T9002 in pSB1A3]	Partsregistry.org	parts.igem.org/Part:BBa_T9002
pJD058 [pKD46 with ampR replaced by kanR]	This paper	N/A
pJD075 [rplQ in T9002 in pSB3T5 backbone]	This paper	N/A
pCDSSara-L17	Shoji et al., 2011 [Peter Schultz Lab]	N/A
pKD46	Datsenko and Wanner, 2000 [Robert Sauer Lab]	N/A

Continued

REAGENT or RESOURCE	SOURCE	IDENTIFIER
pSB1A3	http://parts.igem.org/Main_Page	parts.igem.org/Part:pSB1A3
pSB3T5	http://parts.igem.org/Main_Page	parts.igem.org/Part:pSB3T5
Sequence based reagents		
JDA105: GTGTAGATCACTACTAGAGCCAGGC	This paper	N/A
JDA106: TAATAATACTAGAGCCAG	This paper	N/A
JDA197: GTCGAATAAATACTAGAGTCACACAGG AAAGTACTAGATGCGCCATCGTAAGAGTGGTCG	This paper	N/A
JDA198: AGCCTTTCGTTTTATTTGATGCCTGGC TCTAGTATTATTACTCTGCAGCAGCTTCTGCTT	This paper	N/A
JDA144: CCGCGCCTGGTTGATATCGAGC	This paper	N/A
JDA145: CTGCCCTTTAGTATGCTGATATCG	This paper	N/A
JDA146: TACTAGTAGCGGCCGCTGCAGCTGT CAGACCAAGTTTACTCATATA	This paper	N/A
JDA147: CTAGAAGCGGCCGCGAATTCCAATAT TATTGAAGCATTTATCAGG	This paper	N/A
JDA148: CCTGATAAATGCTTCAATAATATTGGA ATTCGCGGCCGCTTCTAG	This paper	N/A
JDA149: TATATGAGTAAACTTGGTCTGACAGC TGCAGCGGCCGCTACTAGTA	This paper	N/A
Software and Algorithms		
Leginon	National Resource for Automated Molecular Microscopy	http://emg.nysbc.org/redmine/projects/ leginon/wiki/Leginon_Homepage
Appion	National Resource for Automated Molecular Microscopy	http://emg.nysbc.org/redmine/projects/ appion/wiki/Appion_Home
UCSF DRIFTCORR	Li et al., 2013b	cryoem.ucsf.edu/software/driftcorr.html
CTFFind3 and CTFTilt	Mindell and Grigorieff, 2003	grigorieflab.janelia.org/ctf
Manual Masker	National Resource for Automated Molecular Microscopy	http://emg.nysbc.org/redmine/projects/ appion/wiki/Appion_Home
DoG Picker	Voss et al., 2009	emg.nysbc.org/redmine/projects/software/ wiki/DoGpicker
Xmipp CL2D	Sorzano et al., 2010	http://xmipp.cnb.csic.es/twiki/bin/view/ Xmipp/WebHome
FindEM	Roseman, 2004	http://emg.nysbc.org/redmine/projects/ software/wiki/FindEM
Optimod	Lyumkis et al., 2013b	http://emg.nysbc.org/redmine/projects/ appion/wiki/Appion_Home
LM-BFGS Alignparts with Exposure Weighting	Grant and Grigorieff, 2015; Rubinstein and Brubaker, 2015	https://sites.google.com/site/rubinsteingroup/ direct-detector-align_lmbfgs
GCTF	Zhang, 2016	www.mrc-lmb.cam.ac.uk/kzhang/Gctf/
Xmipp projection matching	Sorzano et al., 2004	http://xmipp.cnb.csic.es/twiki/bin/view/ Xmipp/WebHome
Frealign	Grigorieff, 2016; Lyumkis et al., 2013a	grigorieflab.janelia.org/frealign
Relion	Scheres, 2012	https://www2.mrc-lmb.cam.ac.uk/relion/ index.php/Main_Page
EMAN	Ludtke et al., 1999	blake.bcm.edu/emanwiki/EMAN2
ResMap	Kucukelbir et al., 2014	resmap.sourceforge.net/
Chimera	UCSF Resource for Biocomputing, Visualization, and Informatics	www.cgl.ucsf.edu/chimera/
Segger	Pintilie et al., 2010	ncmi.bcm.edu/ncmi/software/segger/
cryo_occ	This paper	https://github.com/williamsonlab/Davis_ Tan_2016

Continued

REAGENT or RESOURCE	SOURCE	IDENTIFIER
SHAPE-Mapper	Siegfried et al., 2014	www.chem.unc.edu/rna/software.html
MSConvert [64-bit]	Proteowizard	proteowizard.sourceforge.net/tools.shtml
TPP Petunia [v. 4.8.0]	Institute for Systems Biology	https://sourceforge.net/projects/sashimi/
xTandem! with k-score plugin	MacLean et al., 2006	https://sourceforge.net/projects/sashimi/
Comet	Eng et al., 2013	https://sourceforge.net/projects/sashimi/
PeptideProphet	Keller et al., 2002	https://sourceforge.net/projects/sashimi/
iProphet	Shteynberg et al., 2011	https://sourceforge.net/projects/sashimi/
MAYU	Reiter et al., 2009	proteomics.ethz.ch/muellelu/web/LukasReiter/Mayu/
ProteinProphet	Nesvizhskii et al., 2003	https://sourceforge.net/projects/sashimi/
SpectraST	Lam et al., 2007	https://sourceforge.net/projects/sashimi/
Skyline	MacLean et al., 2010	skyline.gs.washington.edu/labkey/project/home/software/Skyline/begin.view
ISODIST	Sperling et al., 2008	williamson.scripps.edu/isodist/
massacre	This paper	https://github.com/williamsonlab/Davis_Tan_2016/tree/master/massacre
masse	This paper	https://github.com/williamsonlab/Davis_Tan_2016/tree/master/masse_ms1, https://github.com/williamsonlab/Davis_Tan_2016/tree/master/masse_ms2
spectrast_rt_extract	This paper	https://github.com/williamsonlab/Davis_Tan_2016/tree/master/spectrast_rt_extract
Other		
Homemade holey gold grids	Russo and Passmore, 2014	CF-1.2/1.3-4Au
Quantitative mass spectrometry workflows	This paper	https://github.com/williamsonLab/Davis_Tan_2016/tree/master/qMS_data_sets
Mass spectrometry analysis parameters	This paper	https://github.com/williamsonLab/Davis_Tan_2016/tree/master/qMS_data_sets

CONTACT FOR REAGENT AND RESOURCE SHARING

Further information and requests for reagents may be directed to and will be fulfilled by Lead Contact Dr. James R. Williamson at jrwill@scripps.edu.

METHOD DETAILS

Strain construction

Recombineering plasmid pJD058 was generated from pKD46 (Datsenko and Wanner, 2000) by replacing the ampicillin resistance cassette with a kanamycin resistance gene using Gibson assembly with primers JDA146-149. Strain JD189, which is WT K-12 *E. coli* strain NCM3722, was transformed with plasmid pJD058 and this strain was then transformed with pCDSSara-L17 (Shoji et al., 2011) and selected for both plasmids by growing at 30°C on LB supplemented with kanamycin (50 µg/mL), spectinomycin (100 µg/mL) and glucose (0.4%), resulting in strain JD204. Cells were then made recombinogenic by the addition of 0.2% arabinose for 1 hr before preparing cells for electroporation. A bL17 knockout cassette was generated from genomic DNA isolated from the Shoji Δ*rpl*Q strain via PCR with primers JDA144/145 followed by gel purification. This cassette was electroporated into strain JD204, which was recovered for 2 hr at 30°C on LB supplemented with spectinomycin and 1% arabinose before plating on LB supplemented with spectinomycin, 1% arabinose, and chloramphenicol (35 µg/mL) at 37°C. Colonies were restreaked as above and eventually checked for loss of pJD058 by testing their sensitivity to kanamycin and the correct insertion of the *rpl*Q knockout by sequencing of a PCR product covering the altered region of the genome resulting in strain JD311.

The HSL-inducible bL17 plasmid was generated by Gibson cloning of the bL17 coding sequence in place of the GFP coding sequence in part T9002, which was in the plasmid backbone pSB3T5 (www.partsregistry.org), resulting in the plasmid pJD075. Primers JDA105/106/197/198 were used to generate the requisite PCR products. Strain JD311 was then made chemically competent using TSS [LB supplemented with 0.1 g/mL PEG-8000, 30 mM MgCl₂, 5% DMSO] and transformed with pJD075 and recovered for 1 hr

on LB supplemented with chloramphenicol, spectinomycin, and 1% arabinose before plating on the above media supplemented with tetracycline (10 μg/mL). Colonies were grown on LB supplemented with chloramphenicol, tetracycline, and 5 nM N-(β-Ketocaproyl)-L-homoserine lactone (HSL) to OD_{600} 0.2 before addition of sucrose to 5%. Cells were grown to OD_{600} 1.0 and plated on LB supplemented with chloramphenicol, tetracycline, HSL, and 5% sucrose. Individual colonies were then replica plated with or without spectinomycin to identify colonies lacking the Shoji plasmid and a single spectinomycin-sensitive strain was saved as JD321.

The GFP induction control strain (JD270) was generated by transforming pJD036 [T9002 in the pSB1A3 backbone] into TSS-competent NCM3722 *E. coli* (JD189), and selecting for ampicillin resistance.

Purification of ribosome biogenesis related proteins from the ASKA collection

Ribosome biogenesis-associated proteins (see Key Resources Table) were purified from the ASKA collection overexpression (Kitagawa et al., 2005) library as follows. Cells were grown in 24-well format in 5 mL of LB media supplemented with chloramphenicol (35 μg/mL) to OD ~0.5 before induction with 1 mM IPTG. Cells were harvested 4 hr post-induction by centrifugation at 5,000xg for 15 min and the pellet was saved at −80°C. Each pellet was resuspended in 500μL B-PER (Thermo) supplemented with 1mM PMSF, 2μL benzonase nuclease (Sigma), 0.01mg/mL lysozyme, 5mM β-mercaptoethanol, and incubated for 10 min at 4°C. After centrifugation, the supernatant was applied to 50μL of TALON resin (clonetech) in a 96-well fritted plate. This minicolumn was washed twice with 400μL PBS [10mM NaH_2PO_4, 1.8 mM KH_2PO_4, 140mM NaCl, 3mM KCl; pH 7.4]. Pellet from lysis was washed with 500μL UB1 [10mM NaH_2PO_4, 500mM NaCl, 8M Urea, 5mM β-mercaptoethanol; pH 8.0] and incubated with shaking for 10 min. After centrifugation, the supernatant was added to the TALON resin and the resin was washed three times with 400μL buffer UB1 supplemented with 15mM imidazole. Samples were eluted with via histidine protonation using 500μL buffer EB1 [10 mM NaH_2PO_4, 500 mM NaCl, 8 M urea 10 mM BME; pH 4.5] and the eluent was neutralized using 50μL buffer NB1 [0.5 M NaH_2PO_4; pH 8.0]

Quantitation of growth rates, protein and RNA abundance as a function of HSL

Overnight cultures of JD321 or JD270 were grown in M9 supplemented with tetracycline (10 μg/mL), chloramphenicol (35 μg/mL), and HSL (2 nM) or ampicillin (100 μg/mL) and HSL (2 nM), respectively. Cultures were diluted 1:1,000 into 100 mL cultures with various levels of HSL and grown with aeration (200 rpm) at 37°C. Growth rates and GFP production was quantified via OD_{600} and fluorescence using an EnVision platereader (Perkin Elmer) or by flow cytometry. To determine bL17 levels, 1.5 mL samples were taken at mid-log phase (OD_{600} ~0.3), spiked with a ^{15}N-labeled reference standard lysate and quantified via mass spectrometry as described below.

Cellular protein levels were measured following the Biuret method as follows. First, 1 mL of cell culture was collected at mid-log phase by centrifugation and washed twice with an equal volume of water before resuspension in 0.2 mL water. The sample was then flash-frozen in liquid nitrogen. For analysis, the sample was thawed at room temperature before addition of 0.1 mL NaOH and heating to 100°C for 5 min. Samples were then cooled to room temperature for 5 min in a water bath before addition of 0.1 mL 1.6% $CuSO_4$. After mixing at room temperature for 5 min, samples were centrifuged and the absorbance at 555 nm of the supernatant was measured and compared to that of a standard curve prepared using known concentrations of BSA as described above. Protein concentration was normalized to the OD_{600} of the culture sampled.

Total cellular RNA levels were measured as follows. First, 1.5 mL of cell culture was collected by centrifugation and flash-frozen in liquid nitrogen. After thawing, the pellet was washed twice with 0.6 mL cold 0.1 M $HClO_4$, followed by treatment with 0.3 mL 0.3 M KOH for 60 min at 37°C with constant mixing. Samples were then treated with 0.1 mL 3 M $HClO_4$, and centrifuged at 16,000xg for 10 min. The supernatant was collected and the pellet was washed and collected twice with 0.5 mL 0.5 M $HClO_4$. These supernatants were combined into 1.5 mL total volume and the absorbance at 260 nm was measured.

Cell growth and isolation of ribosomal particles

Strain JD321 was grown under either bL17 permissive (2.0 nM HSL) or non-permissive (0.1 nM HSL) conditions in ^{14}N-labeled supplemented M9 media [48mM Na_2HPO_4, 22mM KH_2PO_4, 8.5mM NaCl, 10mM $MgCl_2$, 10mM $MgSO_4$, 5.6mM glucose, 50μM Na_3·EDTA, 25mM $CaCl_2$, 50μM $FeCl_3$, 0.5μM $ZnSO_4$, 0.5μM $CuSO_4$, 0.5μM $MnSO_4$, 0.5μM $CoCl_2$, 0.04μM d-biotin, 0.02μM folic acid, 0.08μM vitamin B1, 0.11μM calcium pantothenate, 0.4nM vitamin B12, 0.2μM nicotinamide, 0.07μM riboflavin, and 7.6mM $(^{14}NH_4)_2SO_4$] supplemented with 10 μg/mL tetracycline and 35 μg/mL chloramphenicol. Cells were harvested at OD = 0.5 and lysed in Buffer A [20mM Tris-HCl, 100mM NH4Cl, 10mM $MgCl_2$, 0.5mM EDTA, 6mM β-mercaptoethanol; pH 7.5] using a mini bead beater. Clarified lysates (5mL) were fractionated on a 10%–40% w/v sucrose gradient [50mM Tris-HCl, 100mM NH_4Cl, 10mM $MgCl_2$, 0.5mM EDTA, 6mM β-mercaptoethanol; pH 7.5].

Preparation of sample for quantitative mass spectrometry

Individual ^{14}N-labeled fractions were spiked with either a ^{15}N-labeled reference cell lysate purified from JD189 (all fractions) or 70S particles (experimental LSU and 70S peak fractions from permissive and restrictive growth conditions) isolated from strain JD189 as above. Samples were precipitated with 13% TCA at 4°C overnight, pelleted by centrifugation and pellets were successively washed with cold 10% TCA and acetone. Pellets were resuspended in buffer B [100mM NH_4CO_3, 5% acetonitrile, 5mM dithiotreitol]. After incubation for 10 min at 65°C, 10mM iodoacetamide was added, and samples were incubated at 30°C for 30 min. Samples were then digested using 0.2μg trypsin at 37°C overnight.

Quantitative mass spectrometry of ribosomal proteins and assembly factors

Peptides were analyzed on a Sciex 5600+ Triple TOF mass spectrometer coupled to an Eksigent nano-LC Ultra with a nanoflex cHiPLC system as outlined in supplemental workflow 1 (see Key Resources Table). Samples were loaded onto a 200μm x 0.5 mm ChromXP C18-CL 3 μm 120 Å Trap column. Peptides were resolved using a 120 min convex 5%–45% acetonitrile gradient run over a 75 μm x 15 cm ChromXP C-18-CL 3 μm 120 Å analytical column (Gulati et al., 2014). Each sample was injected twice and first analyzed in a data-dependent acquisition mode using a cycle consisting of 250 ms MS^1 followed by 30 successive 100 ms MS^2 scans. Rolling collision energy was utilized. Second, samples were analyzed using a SWATH data independent acquisition scheme consisting of a 200 ms MS^1 followed by 64 100 ms MS^2 scans each isolating a 12.5 Th window ranging from 400 to 1200 Th. Using these datasets, as well as those obtained from whole cell lysates grown at various HSL concentrations (below) and a set of injections using assembly-related proteins purified from the ASKA collection (Kitagawa et al., 2005), data-dependent acquisitions were searched for ^{14}N-labeled peptides against a proteome consisting of *E. coli* (Uniprot UP000000625), a set of common contaminants, and a decoy set of proteins consisting of each protein sequence reversed using Comet (Eng et al., 2013) and x!Tandem with the k-score plugin (MacLean et al., 2006) as outlined in supplemental workflow 2. Search parameters can be found in the Key Resource Table. Peptide probabilities were scored using PeptideProphet and search results were combined via iProphet (Shteynberg et al., 2011) using the Trans-proteomic pipeline. A consensus spectral library was then built using SpectraST (Lam et al., 2007) using a minimum iProb cutoff that corresponded to a protein false discovery rate of ~0.8%, as determined by the MAYU tool. Retention times were normalized using endogenous, high abundance iRT peptides identified previously (Stokes et al., 2014). Well ionized proteotypic peptides lacking spectral interference for ribosomal and assembly factor proteins were identified from the SWATH datasets using Skyline (MacLean et al., 2010), resulting in ~15,000 product ion transitions corresponding to ~3,600 precursor ions, with a light (^{14}N) and heavy (^{15}N) specie measured for each transition. Peptide abundance was calculated as the sum of ^{14}N product ion transitions, divided by the sum of ^{15}N product ion transitions. For ribosomal proteins, this abundance, which was relative to a cell lysate, was converted to that relative to a mature 70S particle using a correction factor determined using the 70S peak fraction from a WT cell analyzed relative to the reference lysate. Peptides analyzed were filtered for mass accuracy, retention time drift, dot product match to spectral library, and ^{14}N/^{15}N spectral dot product. The distribution of these values was inspected on a dataset-by-dataset basis and outliers consisting of ~10% of the total dataset were discarded. Resultant peptides were further filtered for spectral interference by hand. These quantitative workflows are outlined in workflows 3, 5, 5b, 6. Python scripts utilized in these analyses are available at https://www.github.com/williamsonlab/Davis_Tan_2016.

Whole cell proteomics

^{14}N-labeled experimental cultures (1.5 mL) were mixed with a ^{15}N-labeled reference culture composed of JD321 and JD270 cells grown with 0.1 or 2 nM HSL, pelleted and resuspended in 150 μL of 50 mM Tris (pH 8.0). Cultures were lysed by iterative freeze-thaw cycles, pelleted by centrifugation and the supernatant was precipitated with methanol/chloroform [4:1]. After drying, tryptic peptides were generated as described above substituting 0.5 μg of Trypsin/LysC (Pierce) for the described 0.2 μg of Trypsin. Chromatography, data-dependent and SWATH data-independent mass spectrometry, peptide identification, and quantitation were performed as described and are outlined in supplemental workflow 3.

Pulse-labeling proteomics

Samples were pulse-labeled after growing to mid-log phase in ^{14}N-labeled media by the addition of 1 equivalent of ^{15}N-labeled media, resulting in partially labeled peptides. Samples (lysate or purified particles) were then spiked with a ^{15}N-labeled 70S particle as a reference. Data were acquired in data-dependent acquisition mode and searched for ribosomal proteins with Comet and scored with peptideProphet and iProphet. Spectrast was then used to generate a consensus library, which was used to guide the extraction of MS^1 isotope distributions by Massacre (see Key Resources Table). Fits were filtered for isobaric interferences using a series of custom Python scripts. This workflow is outlined in supplemental workflow 4.

SHAPE-MaP based quantitation of rRNA secondary structure

Ribosomal particles were purified on sucrose gradients as described above, concentrations were determined using A$_{260}$, and 10 pmols was incubated for 3 min at 37°C with either 20 mM 1m7 or an equal volume of DMSO in a 450 μL reaction. For each sample, rRNA was purified by Trizol extraction and isopropanol precipitation, and RNA was fragmented by incubation at 95°C in 2.5X 1st strand synthesis buffer (NEB) for 4 min. After fragmentation and purification on a G-50 microspin column (GE Healthcare Life Sciences), reverse transcription reactions were primed with 200 ng of random nonamer primers (NEB) in the presence of MnCl$_2$-bearing RTB [0.7 mM dNTPs, 50 mM Tris-HCl, 75 mM KCl, 6 mM MnCl$_2$, 14 mM DTT] to allow for read-through and introduction of mutations at modified bases. The resulting cDNA library was purified on a G-50 spin column and prepared for Illumina sequencing using NEBNext non-directional 2nd strand synthesis, EndRepair, dA tailing, and TruSeq-barcoded adaptor ligation kits (NEB). Libraries were quality-checked for expected fragment sizes using a BioAnalyzer, before the samples were pooled and gel purified for fragments ~200-500 bp in length. Samples were sequenced on an Illumina HiSeq with unpaired 1x75 bp reads, resulting in ~400 Mb per sample. After quality score and adaptor trimming, reads were aligned to the rrnB P1 transcript sequence, and the per residue mutation rate was determined for each sample analyzed after treatment with either 1M7 (mutR$_{1M7}$) or DMSO (mutR$_{DMSO}$) using the SHAPE-Mapper toolset (Siegfried et al., 2014). For each particle analyzed, residue-specific SHAPE reactivity (SR$_{particle}$) was

calculated as max([mutR$_{1M7}$ - mutR$_{DMSO}$]*1000, 0.0). For 23S rRNA, which was purified from 70S$_{WT}$ particles via Trizol extraction, the per-residue SHAPE reactivity was broken into the following ranges; [SR$_{23S}$ < 1.5] = 0; [1.5 $\leq$ SR$_{23S}$ $\leq$ 3.0] = 3.0; [3.0 < SR$_{23S}$] = 6.0. SHAPE reactivity was plotted on the 23S structure using Mathematica.

Next-generation sequencing based quantitation of rRNA processing

DMSO-treated samples were prepared and sequenced as described above and the number of reads mapped to each residue was determined using SHAPE-Mapper. Reads mapping to immature (residues 2267-2274, 5′; 5179-5187, 3′) or mature termini (residues 2275-2282, 5′; 5170-5178, 3′) were summed and the ratio of immature to mature mapped reads was reported.

Electron microscopy data collection

The LSU$_{bL17dep}$ sample was isolated via sucrose gradient centrifugation (see above) and spin-concentrated using a 100 kDa MW filter (Amicon). 3 μL of this sample were added to plasma cleaned (Gatan, Solarus) 1.2μm hole, 1.3μm spacing holey gold grids (Russo and Passmore, 2014) and plunge frozen into liquid ethane using a Cryoplunge 3 system (Gatan) operating at > 80% humidity, 298K ambient temperature. Single-particle data were collected using the Leginon software package. Data were acquired over two sessions on a Titan Krios microscope (FEI) that is equipped with a K2 summit direct detector (Gatan) operating in counting mode, with a pixel size of 1.31 Å at 22,500x magnification. A dose of 33 to 35 e⁻/Å^2 across 50 frames was used for a dose rate of ∼5.8 e⁻/pix/sec. To compensate for highly preferred orientations, data were collected with tilts ranging from 0° to 60° at 10° increments (Tan et al., unpublished data). A total of 2,479 micrographs were collected.

Electron microscopy micrograph pre-processing and particle stack cleaning

Data processing was performed using several packages incorporated into the Appion pipeline (New York Structural Biology Center). Frames were aligned using UCSF DRIFTCORR software (Li et al., 2013b), and initial CTF estimation on the aligned and summed frames was performed with CTFFind3 and CTFTilt (Mindell and Grigorieff, 2003). Micrographs were visually inspected, and aggregated proteins, regions containing gold substrate, and obvious contamination were masked out using the manual masker in Appion. A total of 84,028 particles from the first dataset were selected *ab initio* using DoG Picker (Voss et al., 2009), extracted and subjected to 2D classification using Xmipp CL2D (Sorzano et al., 2010) to exclude poorly resolved particles. Recognizable class averages, based on visual assessment, were selected and used as templates for a new round of particle selection using FindEM (Roseman, 2004) for both datasets to produce a stack of 447,017 particles. The resulting stack was then subjected to two more rounds of 2D classification using CL2D. The final "clean" stack composed of 131,899 particles resembling ribosomes or ribosomal subunits was exposure filtered (Grant and Grigorieff, 2015) and individual particle "movies" were aligned using local per-particle frame alignment (Rubinstein and Brubaker, 2015). CTF values were then re-estimated on a per-particle basis using GCTF (Zhang, 2016).

Electron microscopy density reconstruction, 3D classification, and refinement

An initial model for the 3D classification was generated using Optimod (Lyumkis et al., 2013b) using the class averages from the final round of CL2D classification from the first dataset. Euler angles and shifts for the particles were determined using Xmipp projection matching (Sorzano et al., 2004) using this initial model as a reference. Iterative 3D classification was then performed using Frealign (Lyumkis et al., 2013a). The initial iteration used 15 classes and ran for 100 rounds. The resulting models were visually examined and grouped according to their similarity; classes inconsistent with a large subunit particle were segregated for later analysis. A total of 5 major classes were identified based on differences in gross structural features. Further sub-classification of 100 iterations was performed on these major classes, targeting between 2 and 6 sub-classes. This number was varied, and a final value was selected such that the classification would produce at least 2 nearly identical models. This strategy indicated that the different 3D classes recovered from the data accurately represented the majority of the real heterogeneity present within the data, at least at the nominal resolution of the reconstructions and using our specific global classification strategy implemented within Frealign. This approach produced a total of 14 different cryo-EM density maps with global resolutions ranging between 4.0 Å to 6.5 Å, including a "70S-like" particle (Figure 3). Global resolutions were determined by masking the two half-maps, calculating the FSC between them using "proc3d" within EMAN and with a cutoff value of 0.143. Masks were generated using Relion by visualizing the map in UCSF Chimera, selecting a threshold for binarization at a contour level that begins to show high-resolution features, extending the mask by 3 pixels and finally appending a soft Gaussian edge of 3 pixels in order to reduce spurious correlations. YjgA densities in D3 and E3 classes were present but weak, indicating that the cofactor is likely to be partially occupied. Determination of the occupancy of YjgA in these classes was carried out using a 3 class multi-model global classification in Frealign (Grigorieff, 2016). For both intermediates, about 30% of the particles had YjgA bound, while 70% did not. Other than YjgA, the rest of the intermediates lacked discernable differences when compared in UCSF Chimera. A second round of 2D classification using Xmipp CL2D in Appion was performed on the excluded particles noted above and a new initial model of these class averages was generated using Optimod. Subsequently, Relion (Scheres, 2012) 5 class multi-model classification was performed on this stack and using the generated initial model, resulting in a single model of the 30S subunit, which was further refined using Frealign to a resolution of 7.9 Å.

B-factor sharpening was performed using bfactor program, which is distributed with Frealign. Classes C1, C2, C3, D1, D2, D3, D4, E1, E2, E3, E4 and E5 were amplitude scaled using diffmap program, also distributed with Frealign, to the lowest resolution 50S

intermediate, class B, for subsequent comparison of protein occupancy. For visualization of the EM maps and generation of figures, UCSF Chimera was used. Local resolution was calculated using the ResMap software (Kucukelbir et al., 2014).

Quantitation of rRNA and protein occupancy in EM density maps

The *E. coli* 50S subunit from the PDB model 4YBB was segmented into 109 separate chains according to rRNA secondary structure maps with an additional chain for each protein (Petrov et al., 2014). Theoretical density was then calculated for each element (helix or protein) at 5 Å using the pdb2mrc command within EMAN (Ludtke et al., 1999). This surface was then binarized at the threshold value 0.026 to generate a mask that was applied to each amplitude-scaled map, and the resulting included volume was calculated using the "volume" command in EMAN (Ludtke et al., 1999). This value was normalized to the total volume of the mask and noted as $vol(j,i)_{init}$ for each class i, and each element j. For each element, final occupancy values, $vol(j,i)_{final}$ were calculated as $vol(j,i)_{init}$/ [max(max($vol(j,i)_{init}$ for all classes), median($vol(j,i)_{init}$ for all classes and all occupied elements]. This value, which scaled from 0 to 1 was also calculated for all threshold values from 0.020 to 0.030 and plotted for each element and each class as a function of threshold. This analysis revealed that the calculated occupancy observed between different classes was insensitive to the threshold used (Figure S6), and the value of 0.026 was selected for all subsequent analyses. Additionally, the calculated occupancy corresponded well to that observed by manual inspection. Element occupancy values were hierarchically clustered across both rows (rRNA/protein elements) and columns (classes) using a euclidean distance metric and complete linkage method (Mathematica).

QUANTIFICATION AND STATISTICAL ANALYSIS

Quantitation of mass spectrometry data detailed above. Statistical values, where calculated, can be found in the Figure legends.

DATA AND SOFTWARE AVAILABILITY

Novel software tools utilized in this manuscript have been deposited at https://www.github.com/williamsonlab/Davis_Tan_2016. All maps are deposited at EMDB as noted in the Key Resources Table. The accession number for the cryo-EM particle stack is EMPIAR: 10076. Processed data files from quantitative mass spectrometry experiments are available in the github repository above as noted in the Key Resources Table.

EXPERIMENTAL MODEL AND SUBJECT DETAILS

E. coli strains were grown supplemented M9 media [48mM Na_2HPO_4, 22mM KH_2PO_4, 8.5mM NaCl, 10mM $MgCl_2$, 10mM $MgSO_4$, 5.6mM glucose, 50μM $Na_3 \cdot EDTA$, 25mM $CaCl_2$, 50μM $FeCl_3$, 0.5μM $ZnSO_4$, 0.5μM $CuSO_4$, 0.5μM $MnSO_4$, 0.5μM $CoCl_2$, 0.04μM d-biotin, 0.02μM folic acid, 0.08μM vitamin B1, 0.11μM calcium pantothenate, 0.4nM vitamin B12, 0.2μM nicotinamide, 0.07μM riboflavin, and 7.6mM $(^{14}NH_4)_2SO_4$] at 37°C in culture flasks ranging in volume from 5 mL test tubes to 2 L baffled flasks. Growth media was supplemented with antibiotics and HSL as noted in the STAR Methods section.
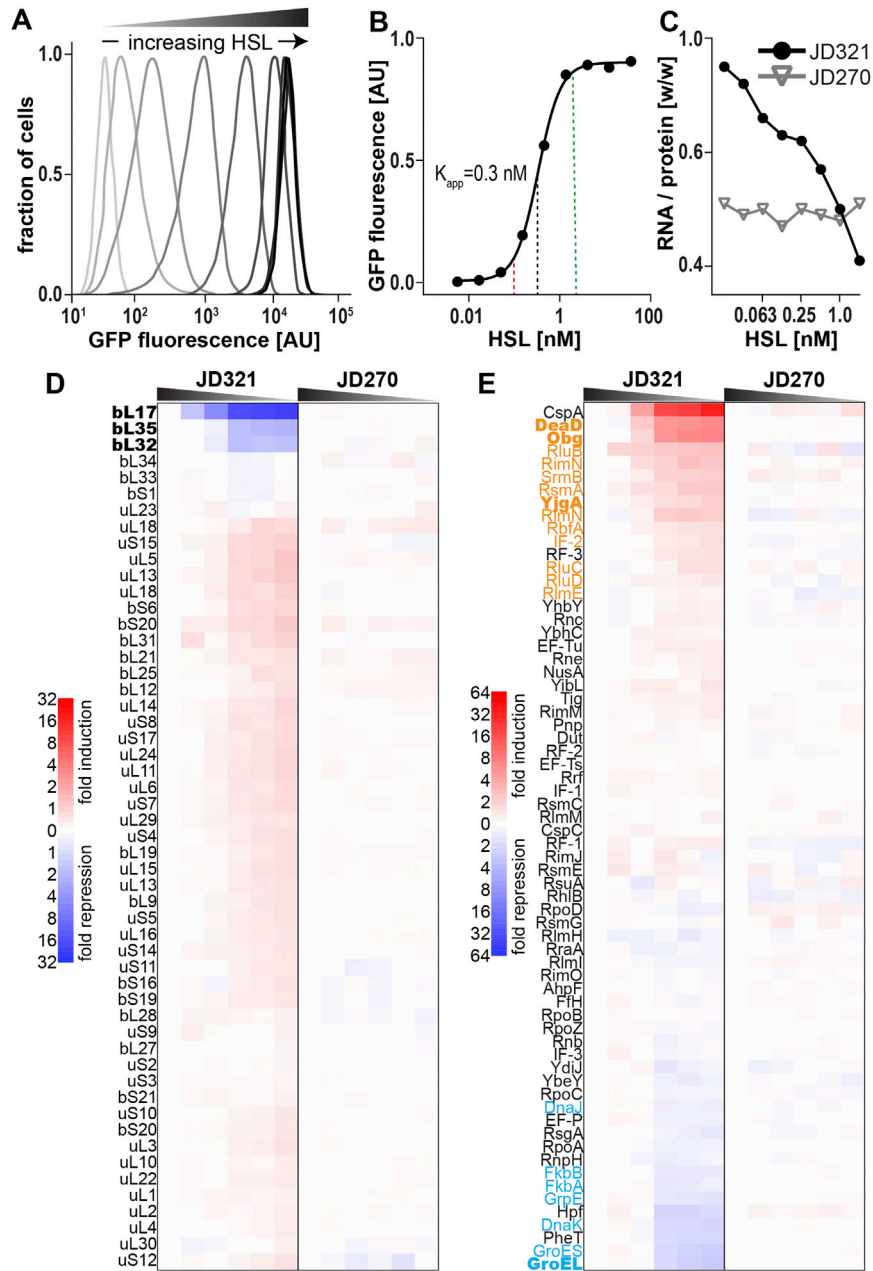
Figure S1. Cellular Response to an R-Protein Limitation, Related to Figure 1

(A) GFP fluorescence intensity flow cytometry histograms as a function of HSL concentration, colored from light gray (0 nM) to black (37 nM).

(B) Median fluorescence intensity values from (A) as a function of HSL concentration fit to the binding function in Equation (1), yielding an apparent dissociation constant, K_{app}, of 0.3 nM (marked with dotted black line) and a Hill coefficient (h) of 1.8. Permissive (2 nM) and restrictive (0.1 nM) HSL concentrations are marked with green and red lines respectively.

$$fl = fl_{max} * \left([HSL]^h \right) \Big/ \left([HSL]^h + K_{app}^h \right) + fl_{min} \tag{1}$$

(C) Ratio of total cellular RNA to protein as a function of HSL concentration in JD321 (black) or control JD270 (gray) cells.

(D and E) (D) Ribosomal protein and (E) assembly factor or chaperone protein levels as measured by qMS, shown as a heatmap, in bL17-limitation JD321 (left) or control JD270 (right) cells as a function of HSL concentration, which ranged from 1.25 nM to 0.039 nM using 2-fold dilutions. For each protein, abundance is normalized to that observed in the 1.25 nM condition and is reported as a fold induction (red) or repression (blue). Proteins individually plotted in Figure 1 are shown in bold. Assembly factors with significant induction are highlighted in orange, and chaperones exhibiting significant repression are highlighted in cyan
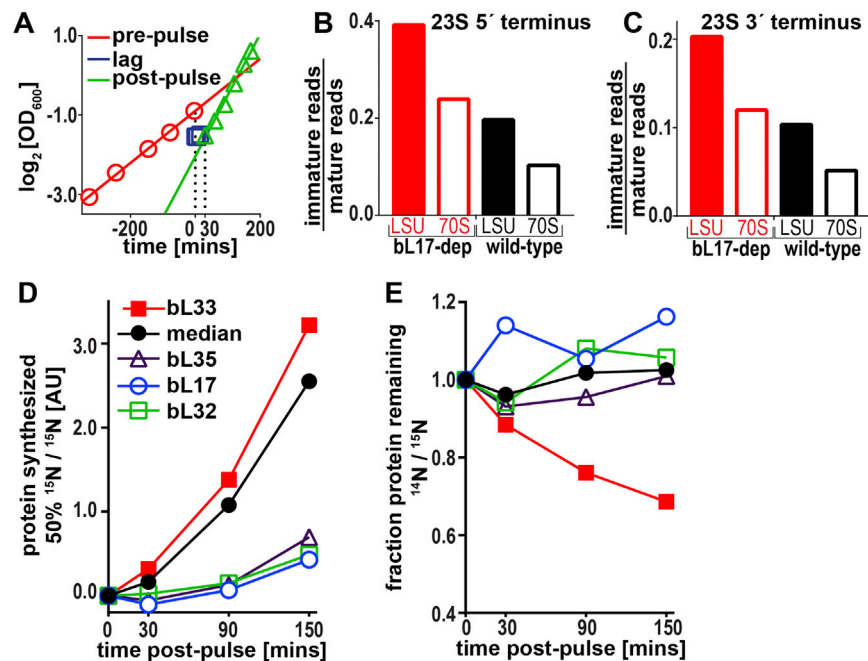
Figure S2. LSU$_{bL17dep}$ Particles Are Maturation-Competent Assembly Intermediates, Related to Figure 2

(A–C) Growth (OD$_{600}$) of JD321 grown under restrictive conditions and pulsed to permissive conditions at time 0. Pre-pulse (red circles) and post-pulse (green triangles) growth were fit to growth rates of 0.0045 and 0.011 min^{-1} respectively. A ~15-30 min lag between these stable regimes (blue squares) is noted by black dotted lines. 23S rRNA maturation state at the 5′ (B) or 3′ (C) termini. LSU (solid) or 70S (outline) particles were isolated from bL17-limited (JD321, 0.1 nM HSL; red) or WT cells (JD189; black) and the ratio of next-generation sequencing reads mapping to rrnB-P1 immature residues (2267-2274, 5′; 5179-5187, 3′) versus those to mature residues (2275-2282, 5′; 5170-5178, 3′) are plotted.

(D) Synthesis rate of ribosomal proteins. bL17-limited cells were pulsed with a stable isotope to quantify protein synthesis using qMS and a fixed reference standard composed of ^{15}N-labeled 70S particles. Newly synthesized (normalized post-pulse isotope label) bL17, bL32, bL33, bL35, and the median LSU r-protein are plotted versus time post-pulse.

(E) Degradation of ribosomal proteins. Cells were grown and pulsed as in (D); however, the normalized pre-pulse isotope level is plotted versus time. Curves labeled as in (D).
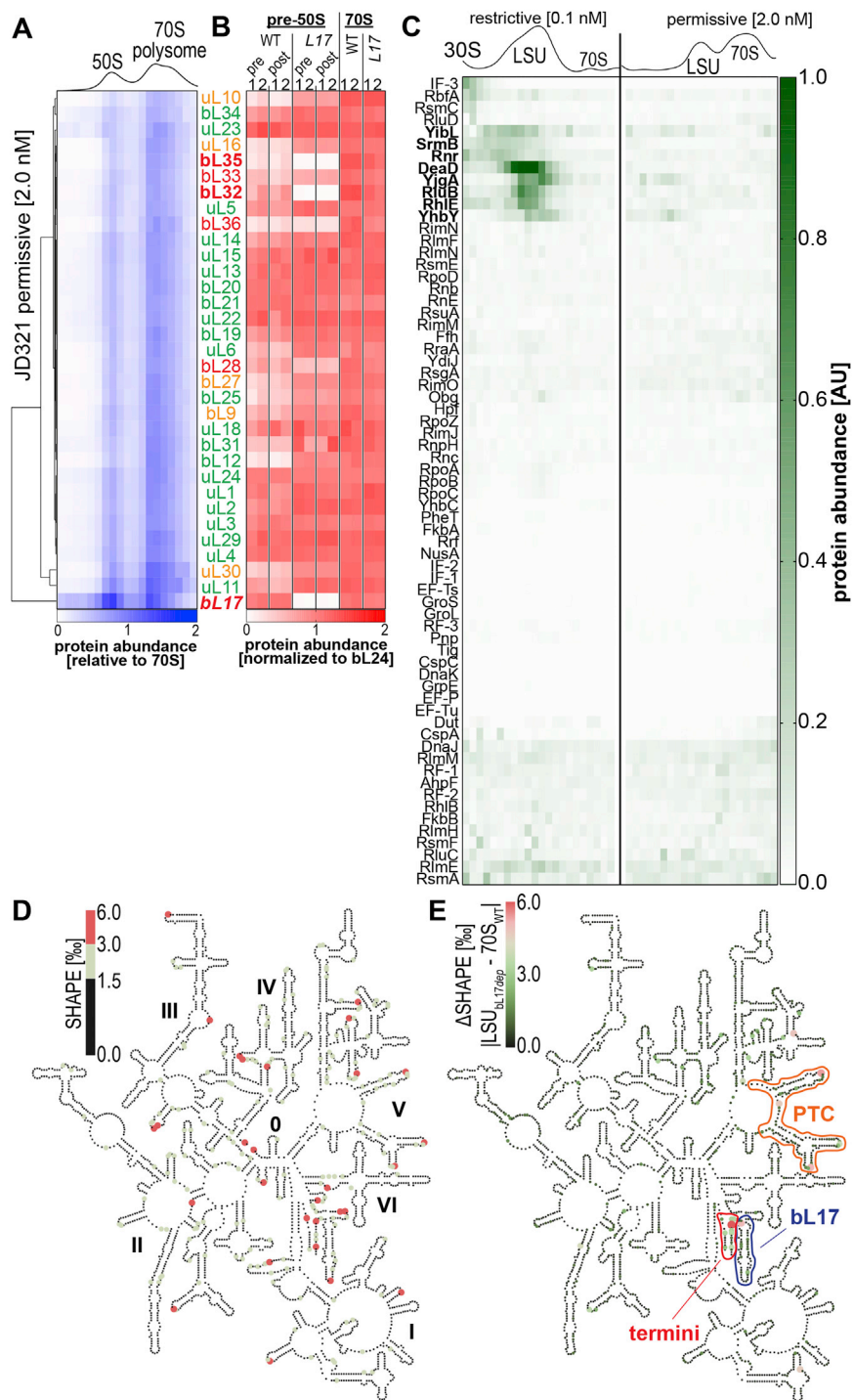
Figure S3. R-Protein Binding Is Re-routed upon bL17 Depletion, Related to Figure 3

(A) Heatmap of LSU protein abundance relative to a purified 70S particle across a sucrose gradient purified from cells grown under bL17-permissive conditions (JD321, 2.0 nM HSL). Occupancy patterns were hierarchically clustered, and protein labels are colored according to the bL17-limited groups from Figure 3A.

(B) Heatmap of LSU protein abundance relative to a 70S particle. Gradients run as in Figure 2A and samples collected at LSU$_{bL17dep}$ region (pre-50S, ~32% sucrose), or from the 70S peak (70S, ~37% sucrose) for either WT cells (JD189) or bL17-restricted cells (JD321, 0.1 nM HSL). Each fraction analyzed in duplicate (1,2). Pre-50S fractions were analyzed before (pre) and after (post) being subjected to concentration in a 100 kDa cutoff spin filter. Abundance in each column was normalized to that of bL24.

(C) Heatmap of ribosome associated protein abundance relative to a fixed cell lysate across sucrose gradients from cells grown under bL17-restrictive or bL17-permissive conditions. Assembly co-factors significantly enriched in the LSU$_{bL17dep}$ particle are in bold. Sucrose gradient profiles depicted above.

(legend continued on next page)

(D) SHAPE reactivity profile resulting from chemical probing of protein-free rRNA mapped onto the 23S secondary structure. SHAPE values represent background corrected mutation rate in per-mille, which has been quantized according to the scale bar. Circles represent individual residues, and their size scales according to SHAPE reactivity. 23S rRNA domains noted (0, I, II, etc.).

(E) SHAPE reactivity differences between $LSU_{bL17dep}$ and $70S_{WT}$ mapped onto the 23S secondary structure. For each particle, SHAPE values calculated as in (D), and the absolute value of the difference is plotted. The 5′ and 3′ 23S termini, the peptidyl transferase center, and a portion of the bL17 binding site are outlined in red, orange, and blue, respectively.
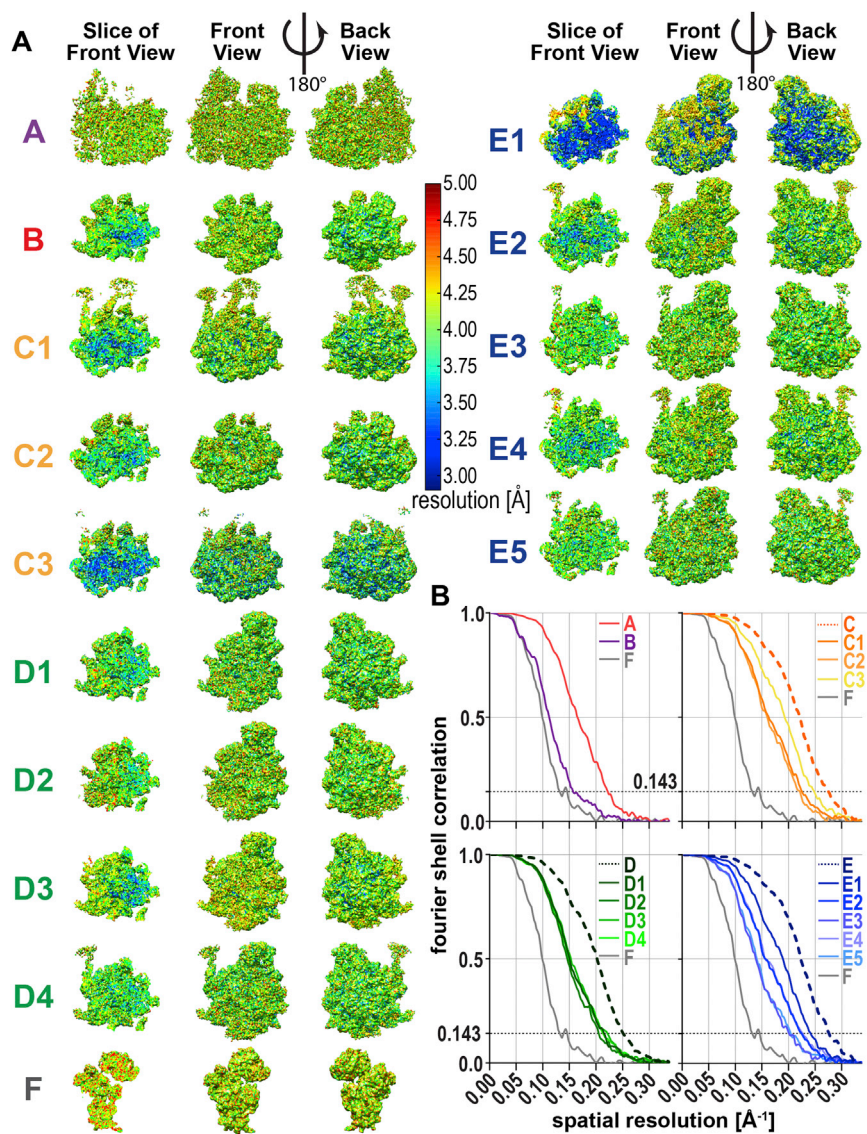
Figure S4. Cryo-EM 3D Classification and Refinement of LSU_{bL17dep} Particles, Related to Figure 4

(A) Local resolution maps for each class generated using ResMap. A longitudinal slice, front view, and back view are shown for each map.

(B) Plots of Fourier shell correlation versus spatial frequency, grouped by super-classes. Class F, the lowest resolution structure obtained, is plotted with each group for comparison. The FSC cutoff of 0.143 was used to report resolution is noted.
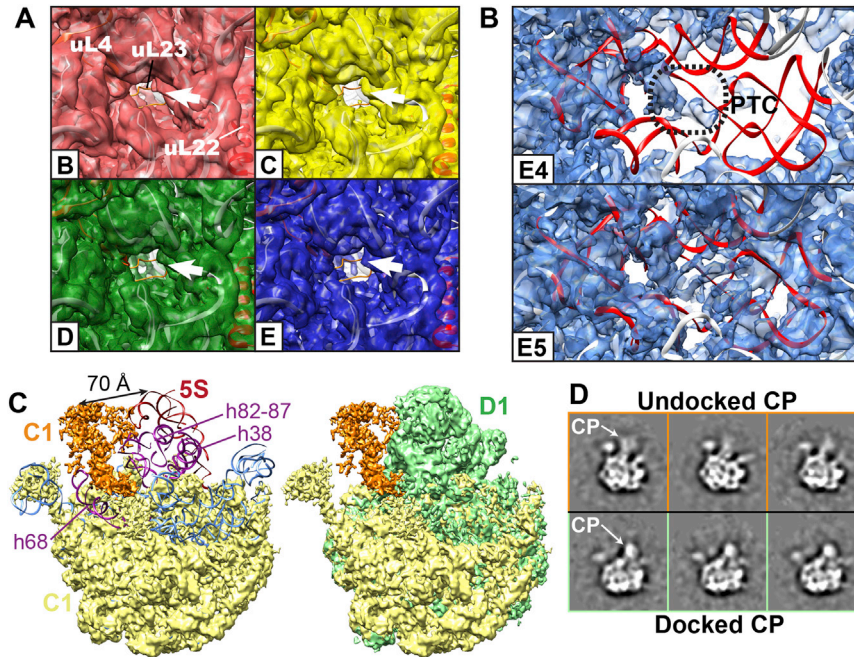
Figure S5. Reconstructed Maps of bL17-Limited Assembly Intermediates, Related to Figure 5

(A) View of the peptide exit channel with each super-class shown as a colored semi-transparent surface. Classes colored as in Figures 4 and 5. Proteins marking the exit tunnel are noted.

(B) Detailed view of the peptidyl transferase center (PTC) disordered (class E4, top) or nearly native (class E5, bottom) confirmation. A-site and P-site rRNA residues colored red.

(C) Maps from classes C1 (orange and yellow) or D1 (green, right) with docked LSU model (PDB: 4YBB, blue). 5S and rRNA helices near the central protuberance (CP) colored red and purple, respectively.

(D) 2D-class averages showing undocked CP (top) or properly docked CP (bottom), which is noted with a white arrow.
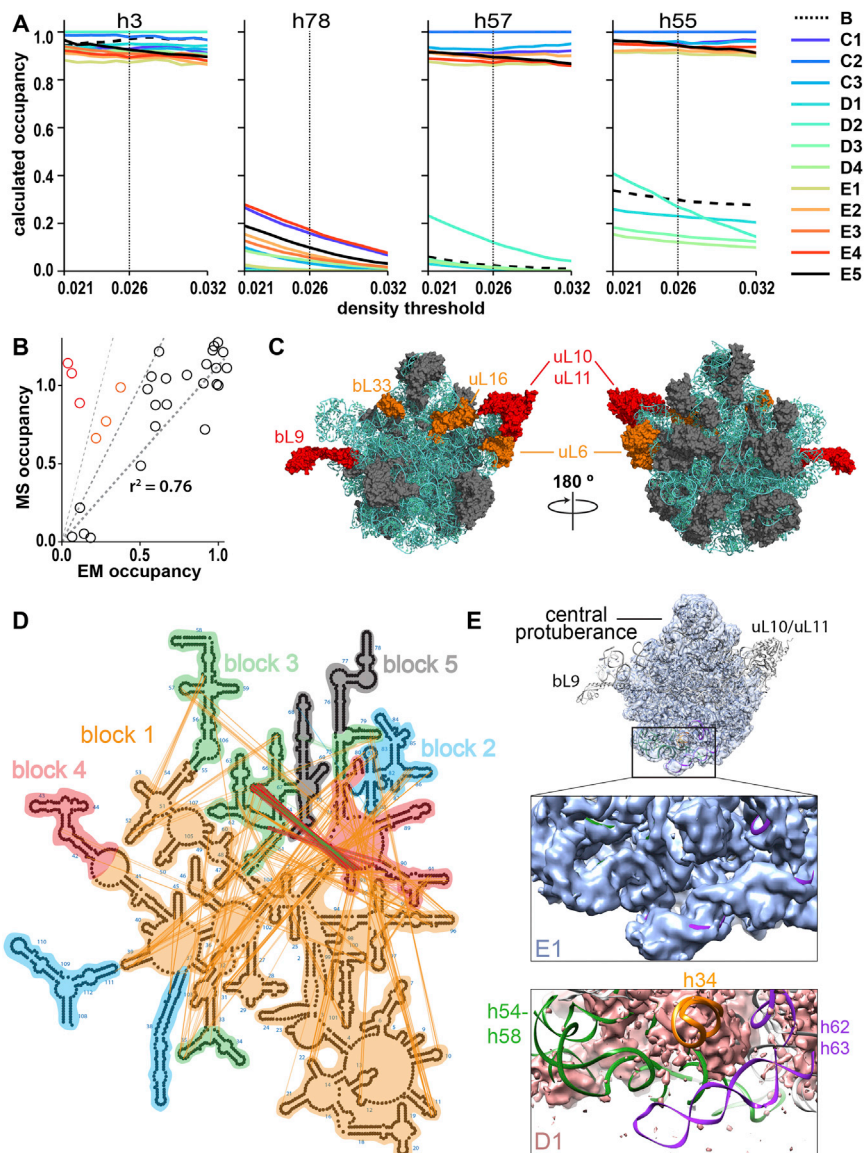
Figure S6. RNA and R-Protein Cooperative Folding Blocks, Related to Figure 6

(A) The sensitivity of the calculated occupancy to the chosen EM density threshold. Representative plots for elements present in all classes (h3, representative of 64/139), absent in all classes (h78, representative of 9/139), differentially present across classes (h57, representative of 61/139) and elements in which apparent occupancy differs between classes dependent on the threshold chosen (h55, representative of 5/139) shown from left to right. Each curve represents the calculated occupancy in a single class and is colored according to the legend at the right. Occupancy calculations in Figure 6 were performed at a threshold of 0.026, which is noted with a dashed vertical line.

(B) Correlation of protein occupancy measured by qMS and by EM. Protein occupancy in EM, which was calculated using the by-class fractional occupancy and the number of particles per class, is plotted against the composite protein occupancy measured in bulk by qMS. Dotted lines indicate a 1:1, 1:2, and 1:4 correspondence between EM and qMS occupancy. Proteins under-represented > 2-fold and > 4-fold by EM are colored orange and red, respectively. Correlation co-efficient for proteins in black noted.

(C) Views of the LSU model (PDB: 4YBB) with proteins under-represented in the EM maps colored according to B), rRNA is cyan and correlated proteins are dark gray.

(D) Tertiary contacts dispensable for cooperative folding blocks. 23S rRNA secondary structure colored and labeled according to blocks from Figure 6A. Tertiary contacts between different blocks (e.g., block 1 to block 2) are colored according to the block that does not require them for folding. Contacts between blocks 2 and 3 are colored with both green and red to indicate the contacts are not necessary for the folding of either domain.

(E) Electron density map in the vicinity of helices 34 (orange), 54-58 (green), and 62-63 (purple), which exhibit differential occupancy between classes E1 (blue, top) and D1 (red, bottom).
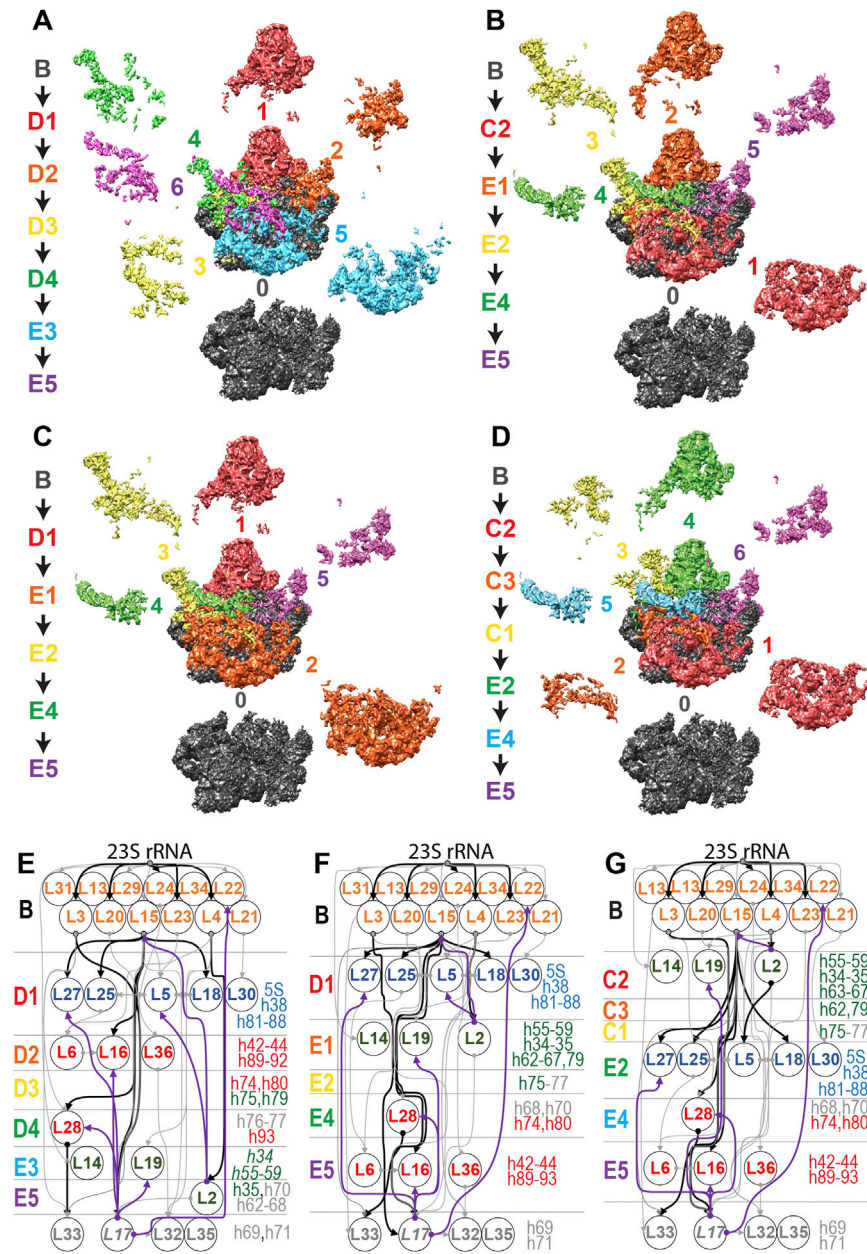
Figure S7. Parallel bL17-Independent Ribosome Assembly Pathways, Related to Figure 7

(A–D) Cryo-EM maps are segmented and colored according to density added during each stage of assembly. For each transition x → y, a difference map y-x is calculated and displayed surrounding the terminal structure. Initial and terminal structures B and E5 are fixed in gray and purple respectively, and remaining difference maps are colored according to assembly order. Numbers indicate the order of structure formation. Representative pathways from Figure 7 are illustrated.

(E–G) Nierhaus assembly map extended to include rRNA helices that cooperatively fold with r-proteins. Nierhaus assembly maps are depicted for three representative assembly pathways from Figure 7. Strong (black) and weak (gray) thermodynamic cooperativities noted with arrows and rRNA helices formed at each transition listed to the right. R-protein interactions from the Nierhaus map that are dispensable in each pathway are highlighted with purple arrows. Proteins and helices are colored according to occupancy groups from Figure 6.